
Restoration Score Distillation: From Corrupted Diffusion Pretraining to One-Step High-Quality Generation

Yasi Zhang^{*,1}, Tianyu Chen^{*,2}, Zhendong Wang³, Ying Nian Wu¹,
Mingyuan Zhou^{†,2}, Oscar Leong^{†,1}

*Equal contribution †Equal advising

¹University of California, Los Angeles ²University of Texas at Austin ³Microsoft
yasminzhang@ucla.edu, tianyuchen@utexas.edu

Abstract

Learning generative models from corrupted data is a fundamental yet persistently challenging task across scientific disciplines, particularly when access to clean data is limited or expensive. Denoising Score Distillation (DSD) [6] recently introduced a novel and surprisingly effective strategy that leverages score distillation to train high-fidelity generative models directly from noisy observations. Building upon this foundation, we propose *Restoration Score Distillation* (RSD), a principled generalization of DSD that accommodates a broader range of corruption types, such as blurred, incomplete, or low-resolution images. RSD operates by first pretraining a teacher diffusion model solely on corrupted data and subsequently distilling it into a single-step generator that produces high-quality reconstructions. Empirically, RSD consistently surpasses its teacher model across diverse restoration tasks on both natural and scientific datasets. Moreover, beyond standard diffusion objectives, the RSD framework is compatible with several corruption-aware training techniques such as Ambient Tweedie, Ambient Diffusion, and its Fourier-space variant, enabling flexible integration with recent advances in diffusion modeling. Theoretically, we demonstrate that in a linear regime, RSD recovers the eigenspace of the clean data covariance matrix from linear measurements, thereby serving as an implicit regularizer. This interpretation recasts score distillation not only as a sampling acceleration technique but as a principled approach to enhancing generative performance in severely degraded data regimes.

1 Introduction

Learning from corrupted data remains a central and challenging problem in many scientific domains where access to clean data is limited or costly, including astronomy [32, 22], medical imaging [31, 18], and seismology [26, 30]. For example, in medical imaging, acquiring fully-sampled MRI scans is not only expensive but can also cause discomfort or require prolonged scanning times for patients [21, 47]. Hence, an important challenge in these domains is to learn the structure of the underlying ground-truth data directly from corrupted observations. In this work, we will consider the question of generative modeling from corruption. Formally, given a clean data point $x \in \mathbb{R}^d$ sampled from an unknown distribution p_X , we are given corrupted samples of the form

$$y = \mathcal{A}(x) + \sigma\epsilon, \quad \epsilon \sim \mathcal{N}(0, I_m), \quad (1)$$

where $\mathcal{A} : \mathbb{R}^d \rightarrow \mathbb{R}^m$ represents a corruption operator and σ denotes the noise level. The operator \mathcal{A} may induce dimensionality reduction or blurring through linear transformations, or more complex

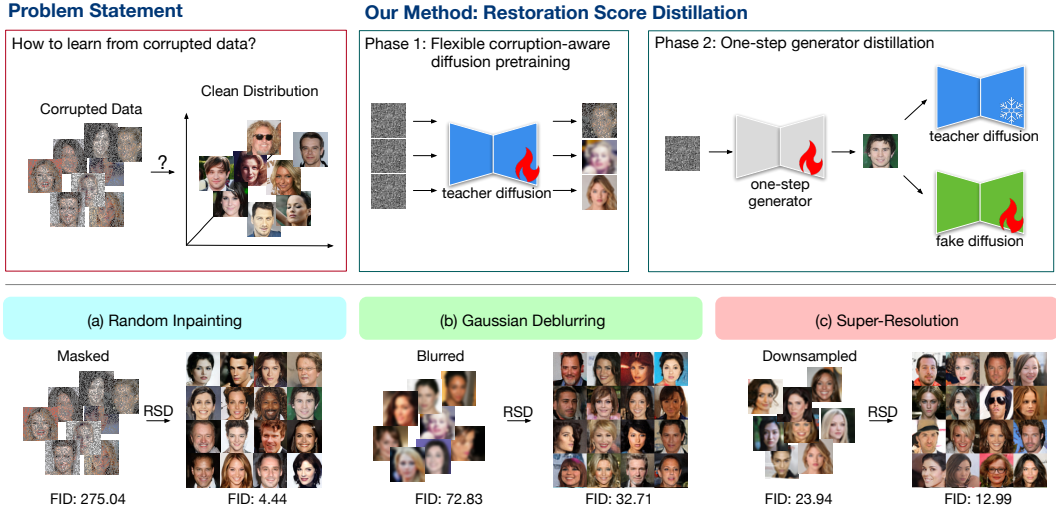


Figure 1: Illustration of our RSD framework and its results across diverse restoration tasks, including Gaussian deblurring, random inpainting, and super-resolution. Additional qualitative examples are provided in Appendix A.

effects such as nonlinear distortions. The key objective is to recover the underlying distribution p_X of clean data from only corrupted observations $\{y^{(i)}\}_{i=1}^N$ of the form (1).

To address this, there is growing interest in training generative models, particularly diffusion models, under corruption. Diffusion models [36, 16], also known as score-based generative models [37, 38], have become the leading paradigm for modeling high-dimensional continuous data, particularly high-resolution images [13, 17, 29, 33, 35, 27, 51, 50, 4]. Among existing strategies, Ambient Tweedie [11] and Ambient Diffusion [9] use corruption-aware objectives to learn clean priors, although their applicability is typically limited to denoising and inpainting tasks, respectively. Another approach, EM-Diffusion [3], adopts an Expectation-Maximization framework [1] that alternates between reconstructing clean samples using a fixed diffusion model and updating model weights with the reconstructions. While broadly applicable to various corruption operators, EM-Diffusion requires pretraining with a small clean dataset and often suffers from local optima, high computational cost, and degraded performance in severely corrupted regimes.

A recent study [6] introduced a novel and surprisingly effective approach for training high-quality generative models from noisy data via Denoising Score Distillation (DSD). Diffusion distillation [28, 42, 24, 46, 52, 43–45] is commonly regarded as a mechanism for accelerating a pretrained (or teacher) diffusion model into a single-step generator while preserving sample fidelity. However, Chen et al. [6] reveals that, particularly under noisy training conditions, score distillation can go beyond acceleration and lead to significant improvements in sample quality.

In this work, we propose *Restoration Score Distillation* (RSD), a principled extension of DSD designed to handle a broader class of corruptions, including blurred, incomplete, and low-resolution images. RSD first pretrains a diffusion model exclusively on corrupted observations, then distills it into a one-step generator capable of producing clean and refined samples. Across a range of corruption operators, whether noisy or noiseless, and on diverse datasets including natural images (e.g., CelebA-HQ [23, 19]) and scientific images (e.g., FastMRI [21, 47]), RSD consistently enhances generative performance relative to its teacher diffusion model. These findings suggest that, when appropriately harnessed through score distillation, corrupted data can yield more informative supervision than previously recognized. Moreover, the RSD framework is compatible with several corruption-aware training techniques such as Ambient Tweedie [11], Ambient Diffusion [8], and Fourier-space Ambient Diffusion [2], enabling flexible integration with recent advances in diffusion modeling.

To explain this phenomenon, we provide a theoretical analysis in Sec. 4, showing that, in a linear model setting, a distilled student model learns superior representations by aligning with the eigenspace of the underlying clean data distribution’s covariance matrix when given access to the corrupted distribution’s score. This insight confirms that score distillation not only as an acceleration tool but also as a theoretically grounded mechanism for improving generative models trained on corrupted data.

Our key contributions can be summarized as follows:

- We propose *Restoration Score Distillation* (RSD), a general framework for training generative models from corrupted data without any access to clean samples, extending the scope of score distillation beyond denoising (i.e., DSD) to broader corruption types including blurring, inpainting, and low-resolution degradation. See Fig. 1 for our method’s workflow.
- RSD unifies and improves upon existing advanced corruption-aware diffusion training techniques such as Ambient Tweedie, Ambient Diffusion, and its Fourier-space variant, by distilling a teacher diffusion model trained solely on corrupted data into a one-step generator, achieving superior performance across multiple datasets and corruption settings.
- We provide a theoretical justification showing that, in the linear regime, RSD implicitly recovers the eigenspace of the clean data distribution, thereby offering a principled interpretation of score distillation as both an acceleration and regularization mechanism.

2 Background

2.1 Diffusion Models

Diffusion models [36, 16], also known as score-based generative models [37, 38], consist of a forward process that gradually perturbs data with noise and a reverse process that denoises this signal to recover the data distribution $p_X(x)$. Specifically, the forward process defines a family of conditional distributions over noise levels $t \in (0, 1]$, given by $q_t(x_t | x) = \mathcal{N}(\alpha_t x, \sigma_t^2 I)$, with marginals $q_t(x_t)$. We adopt a variance-exploding (VE) process [37] by setting $\alpha_t = 1$, yielding the simple form $x_t = x + \sigma_t \epsilon$, where $\epsilon \sim \mathcal{N}(0, I_d)$. To model the reverse denoising process, one typically trains a time-dependent denoising autoencoder (DAE) $f_\phi(\cdot, t) : \mathbb{R}^d \times [0, 1] \rightarrow \mathbb{R}^d$ [41], parameterized by a neural network, to approximate the posterior mean $\mathbb{E}[x | x_t]$. This is achieved by minimizing the following empirical objective:

$$\ell(\phi; \{x^{(i)}\}_{i=1}^N) := \frac{1}{N} \sum_{i=1}^N \int_0^1 \mathbb{E}_{\epsilon \sim \mathcal{N}(0, I_d)} \left[\left\| f_\phi(x^{(i)} + \sigma_t \epsilon, t) - x^{(i)} \right\|^2 \right] dt, \quad (2)$$

where $\{x^{(i)}\}_{i=1}^N$ denotes the dataset of clean training samples. For clarity, we omit weighting functions over t , which are often used in practice to prioritize certain noise levels, in this paper.

2.2 Diffusion Models for Corruptions

Recent works extend diffusion models to handle diverse practical data corruptions. We introduce Ambient Tweedie, Ambient Diffusion, and Fourier-Space Ambient Diffusion as follows.

Ambient Tweedie for Noisy Corruptions. Ambient Tweedie [11] generalizes score matching to noisy observations $y = \mathcal{A}(x) + \sigma \epsilon$, where \mathcal{A} is a linear operator and $\epsilon \sim \mathcal{N}(0, I)$. Here, $\sigma > 0$ is a known noise level in the measurements with fixed timestep $t_\sigma \in (0, 1]$. One can incorporate the known corruption by minimizing

$$\ell_{\text{tweedie}}(\phi; \{y^{(i)}\}_{i=1}^N) = \frac{1}{N} \sum_{i=1}^N \int_{t_\sigma}^1 \mathbb{E}_{\epsilon \sim \mathcal{N}(0, I_m)} \left\| \frac{\sigma_t^2 - \sigma^2}{\sigma_t^2} f_\phi(w_t^{(i)}, t) + \frac{\sigma^2}{\sigma_t^2} w_t^{(i)} - y^{(i)} \right\|^2 dt, \quad (3)$$

where $w_t^{(i)} = y^{(i)} + \sqrt{\sigma_t^2 - \sigma^2} \epsilon$. This formula ultimately models the distribution of the corrupted but noiseless data $w = \mathcal{A}(x)$.

Ambient Diffusion for Masked Observations. Ambient Diffusion [9] addresses partial observations such as image inpainting by integrating masking into the training objective. Given masked observations $y = Mx$ with a binary mask operator M , the model is trained by:

$$\ell_{\text{ambient}}(\phi; \{y^{(i)}\}_{i=1}^N) = \frac{1}{N} \sum_{i=1}^N \int_0^1 \mathbb{E}_{\tilde{M}^{(i)}, \epsilon \sim \mathcal{N}(0, I_d)} \left\| M^{(i)} \left(f_\phi(\tilde{M}^{(i)} x_t^{(i)}, t) - y^{(i)} \right) \right\|^2 dt, \quad (4)$$

where \tilde{M} is a secondary random mask to further obscure the already-masked input, ensuring that the model learns to infer missing information rather than merely copying observed values.

Fourier-Space Ambient Diffusion for Frequency-Domain Corruptions. Designed for scientific imaging (e.g., MRI), this variant [2] adapts Ambient Diffusion to handle masked observations in the frequency domain, where observations are $y = M\mathcal{F}x$, and \mathcal{F} denotes the Fourier transform operator. Please refer to Appendix E.4 for more details.

These specialized frameworks enable generative modeling from realistic scenarios such as blurring, missing data, or frequency-domain degradation.

2.3 Score Distillation for Generative Modeling

Score distillation converts multi-step diffusion models into efficient single-step generative models. Initially developed for tasks like text-to-3D generation [28, 42] and later extended to image synthesis [24, 46, 52, 43], it transfers knowledge from a pretrained diffusion (teacher) model f_ϕ to a simpler generator $G_\theta : \mathbb{R}^d \rightarrow \mathbb{R}^d$, enabling rapid sampling. An auxiliary “fake” diffusion model $f_\psi(x_t, t)$ approximates the generator-induced distribution at different corruption levels. Given a fixed teacher model f_ϕ , the distillation minimizes the divergence between teacher and fake distributions:

$$\mathcal{J}(\theta; \psi) = \mathbb{E}_{z \sim \mathcal{N}(0, I_d), x = G_\theta(z)} \left[\int_0^1 \mathcal{D}(p_{\psi,t}(x_t), p_{\phi,t}(x_t)) dt \right], \quad (5)$$

Here, $\mathcal{D}(\cdot, \cdot)$ typically denotes a divergence measure such as KL or Fisher divergence. In our work, we adopt Fisher divergence, as introduced in the SiD framework [52], to instantiate the distillation loss for both theoretical analysis and experimental design. A detailed discussion is in Appendix F.

3 Restoration Score Distillation

Problem Statement. Suppose we are given a finite, fixed corrupted dataset of size N , denoted by $\{y^{(i)}\}_{i=1}^N$. Each corrupted observation is generated as $y^{(i)} = \mathcal{A}(x^{(i)}) + \sigma\epsilon^{(i)}$, where σ is a known noise level, and $\epsilon^{(i)} \stackrel{\text{i.i.d.}}{\sim} \mathcal{N}(0, I_m)$. Importantly, the clean data $\{x^{(i)}\}_{i=1}^N$ is not accessible at any time. We note that in some cases (e.g., random inpainting), \mathcal{A} is not fixed but may instead vary across data samples, following the same distribution. As a result, we have $y^{(i)} = \mathcal{A}^{(i)}(x^{(i)}) + \sigma\epsilon^{(i)}$.

RSD is a two-phase framework that enables learning generative models solely from corrupted observations. It decouples the learning process into: (1) a flexible corruption-aware diffusion pretraining stage, and (2) a distillation stage that compresses the pretrained model into a single-step generator. The algorithm is summarized in Algorithm 6 in the Appendix.

3.1 Phase I: Flexible Corruption-Aware Pretraining

The first phase involves training a teacher diffusion model $f_\phi(\cdot, t)$ directly on corrupted observations $y = \mathcal{A}(x) + \sigma\epsilon$, where \mathcal{A} is a potentially non-invertible corruption operator. A naive approach is to train the model on corrupted data y using the standard diffusion loss (2) (see Algorithm 1, Appendix E.1 for details). In our experiments, we find that using the standard diffusion loss already yields strong performance. To further enhance results across various corruption operators and scenarios, we explore existing corruption-aware diffusion training strategies, as summarized in Tab. 1.

We describe our choice of pretraining objectives for different corruption scenarios as follows: 1) **Standard Diffusion** is effective for general corruption operators under a noiseless setting. It directly models the distribution of $y = \mathcal{A}(x)$. 2) **Ambient Tweedie** [11] is designed for scenarios with additive noise. It improves performance by learning to model the distribution of $\mathcal{A}(x)$ from noisy observations $y = \mathcal{A}(x) + \sigma\epsilon$, providing an implicit denoising effect. 3) **Ambient Diffusion** [9] is a diffusion training strategy tailored for random inpainting tasks. It aims to learn the distribution of x from partial observations Mx , where M denotes a random inpainting mask. 4) **Fourier-Space Ambient Diffusion** [2] extends Ambient Diffusion to Fourier-domain corruptions. It is particularly suited for frequency-based degradation, such as in medical imaging tasks where full-sampled MRI acquisitions are costly and time-consuming. This method learns the distribution of x from masked Fourier observations $M\mathcal{F}x$.

We summarize all variants of diffusion training methods in Tab. 1. In the experiments section, we present all distillation results using different pretraining objectives, each tailored to a specific scenario.

Table 1: Summary of corruption-aware diffusion objectives used for pretraining. Our framework can be seamlessly integrated with existing advanced corruption-aware diffusion objectives.

Pretraining Objective	Suitable Scenario	Operator	Domain
Standard Diffusion	Noiseless	$\mathcal{A}(x)$	Image space
Ambient Tweedie	Noisy	$\mathcal{A}(x) + \sigma\epsilon$	Image space
Ambient Diffusion	Masked	Mx	Image space
F.S. Ambient Diffusion	Masked	$M\mathcal{F}x$	Fourier space

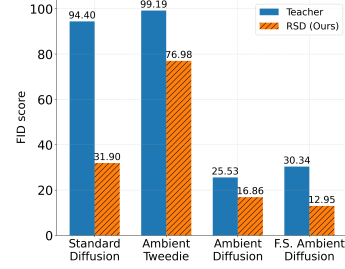


Figure 2: RSD vs Teacher Models

To provide a concise overview, we highlight the superior performance of our RSD model over its teacher model in Fig. 2. These four objectives correspond to the following tasks: noiseless Gaussian deblurring, noisy Gaussian deblurring, random inpainting, and multi-coil MRI reconstruction. **Our framework allows users to select the most appropriate objective based on the type of corruption, offering a unified pretraining strategy for a wide range of image restoration tasks.** A more detailed description of these tasks is provided in Sec. 5.

3.2 Phase II: One-Step Generator Distillation

After pretraining, we distill the teacher diffusion model f_ϕ into a one-step generator G_θ , such that $G_\theta(z)$, $z \sim \mathcal{N}(0, I_d)$, directly produces samples resembling clean data. The distillation process introduces a surrogate diffusion model $f_\psi(\cdot, t)$, which is initialized from the teacher and trained on corrupted outputs of G_θ to align its time-dependent behavior with that of the teacher.

We adopt the SiD [52] framework for distillation, which uses Fisher divergence as the training objective by default, as it has been shown to stabilize the distillation process and yield superior performance compared to KL divergence [6]. A detailed discussion of the distillation loss and its formulation is provided in Appendix F. Beyond standard score distillation, our method further corrupts the generated samples into \tilde{y} in the same manner as the corruption of the training dataset, as illustrated in Line 13/17 of Algorithm 6. These corrupted samples are then used to train a fake diffusion model $f_\psi(\cdot, t)$ and one-step generator $G_\theta(\cdot)$.

4 Theoretical Analysis

For our theoretical analysis, we aim to understand the type of generative model that is learned when given access to the score function of the corrupted data distribution. To this end, we consider a simplified linear model setting. We will show that the distilled generator achieves a smaller Wasserstein distance to the true clean distribution p_X compared to the pretrained diffusion model.

Assumption 1 (Linear Low-Rank Data Distribution). *Suppose our underlying data distribution is given by a low-rank linear model $x = Ez \sim p_X$ and $z \sim \mathcal{N}(0, I_r)$, where $E \in \mathbb{R}^{d \times r}$ with $r < d$ and with orthonormal columns (i.e. $E^T E = I_r$).*

By Assumption 1, it is clear that $p_X := \mathcal{N}(0, EE^T)$ is a degenerate low-rank Gaussian distribution. For a fixed corruption noise level $\sigma > 0$, consider the setting we only have access to the noisy distribution $y = \mathcal{A}(x) + \sigma\epsilon$, where $\epsilon \sim \mathcal{N}(0, I_m)$ and $\mathcal{A}(x) = Ax$ with $A \in \mathbb{R}^{m \times d}$ is a linear corruption operator. By our assumption on p_X and the noise, $p_{Y,\sigma} := \mathcal{N}(0, AEE^T A^T + \sigma^2 I_m)$. In order to get rid of error in estimating score, we assume that we have perfectly learned the noisy score:

Assumption 2 (Perfect Score Estimation). *Suppose $A \in \mathbb{R}^{m \times d}$ with $\text{rank}(A) = m$ and we can estimate the score function of corrupted data y perfectly:*

$$s_{A,\sigma^2}(x) := \nabla \log p_{Y,\sigma^2}(x) = -(AEE^T A^T + \sigma^2 I_m)^{-1} x.$$

Our goal is to distill this distribution into a distribution $p_{G_\theta} := (G_\theta)_\# \mathcal{N}(0, I_d)$ given by the push-forward of $\mathcal{N}(0, I_d)$ by a generative network $G_\theta : \mathbb{R}^d \rightarrow \mathbb{R}^d$. To model a U-Net [34] style architecture with a low-rank structure, we assume G_θ satisfying the property in Assumption 3.

Assumption 3 (Low-Rank Linear Generator). Assume the generator follows a low-rank linear mapping, where G_θ is parameterized by $\theta = (U, V)$ with $U, V \in \mathbb{R}^{d \times r}$ and has the form:

$$G_\theta(z) := UV^T z, \text{ where } z \sim \mathcal{N}(0, I_d).$$

Note that G_θ induces a degenerate low-rank Gaussian distribution $p_{G_\theta} := \mathcal{N}(0, UV^T VU^T)$. Our goal is to match the corrupted noise distribution’s score with the score of p_{G_θ} corrupted by A over a series of noise schedules (σ_t) , which is given by

$$\tilde{p}_{G_\theta}^{\sigma_t}(y) = \mathcal{N}(0, AUV^T VU^T A^T + \sigma_t^2 I_m).$$

To distill the noisy distribution, we minimize the score-based loss (or Fisher divergence) as in [52]:

$$\mathcal{L}(\theta) := \mathbb{E}_{t \sim \text{Unif}[0,1]} \mathbb{E}_{y_t \sim \tilde{p}_{G_\theta}^{\sigma_t}} \left[\|s_{A, \sigma^2 + \sigma_t^2}(y_t) - \nabla \log \tilde{p}_{G_\theta}^{\sigma_t}(y_t)\|_2^2 \right]. \quad (6)$$

We show that we can characterize the global minimizers of this loss, which correspond to a noise-dependent scaling of the *true* eigenspace of p_X plus perturbations in the kernel of A . If we penalize the norm of our solution, we can nearly recover the true data distribution in Wasserstein-2 distance up to the noise in our measurements. We consider the rank- $r = 1$ case for simplicity.

Theorem 1. Fix $\sigma > 0$ and consider $e \in \mathbb{R}^d$ with unit norm and $Ae \neq 0$. Under Assumptions 1, 2, and 3 and any bounded noise schedule $(\sigma_t) \subseteq [\sigma_{\min}, \sigma_{\max}]$, the set of global minimizers of the loss (6) under the parameterization $u \mapsto \theta(u) = (u, u/\|u\|)$ is given by

$$\Theta_* := \left\{ \pm \sqrt{1 + \frac{\sigma^2}{\|Ae\|^2}} \cdot e \right\} + \ker(A).$$

If $e \in \text{Im}(A^T)$, we have that $\theta_* = \theta_*(u_*)$ with the minimum norm solution $u_* \in \text{argmin}_{u \in \Theta_*} \|u\|$ satisfies

$$W_2^2(p_X, p_{G_{\theta_*}}) = \left(\sqrt{1 + \frac{\sigma^2}{\|Ae\|^2}} - 1 \right)^2.$$

5 Experiments

We conduct comprehensive experiments to evaluate the effectiveness, flexibility, and generality of our proposed framework, RSD, across both natural and scientific imaging domains. Our evaluations cover a wide range of challenging image restoration tasks including Gaussian deblurring, random inpainting, and super-resolution on the CelebA-HQ 64×64 dataset [23, 19] under both noiseless ($\sigma = 0.0$) and noisy ($\sigma = 0.2$) settings. To further assess its real-world applicability, we apply RSD to multi-coil Magnetic Resonance Imaging (MRI) using the FastMRI dataset [47, 21], where fully sampled ground truth is often unavailable. Across all tasks and corruption settings, RSD consistently outperforms the teacher diffusion models, achieving superior generative quality as measured by FID [14], and surpasses recent baselines such as EM-Diffusion (few-shot, using 50 clean images) [3], all while requiring no access to clean data. We also show that RSD can be directly distilled from existing pretrained teacher models with advanced corruption-aware techniques, including Ambient Tweedie [11], Ambient Diffusion [8], and its Fourier-space variant [2], demonstrating the flexibility and modularity of our framework. Last but not least, RSD enjoys high distillation data efficiency (Section 5.4), surpassing the performance of teacher diffusion models swiftly, as well as high inference efficiency due to the distillation nature ($25\times$ speedup; see Appendix G.2). Detailed implementation details are provided in Appendix G.

5.1 Natural Images

Baseline methods. We compare our method with three baseline methods to evaluate generative performance: 1) **Standard Diffusion** [20] (Appendix E.1): The teacher model trained with standard diffusion loss (2) under the noiseless setting serves as a generative baseline. 2) **Ambient Tweedie** [10, 11] (Appendix E.2): When additive noise exists, Ambient Tweedie loss (3) improves over standard diffusion by learning an unbiased score of corrupted but noiseless data. We follow [11] and

Table 2: **Results of our method RSD on CelebA-HQ across various restoration tasks under both noiseless and noisy settings.** Baselines results are taken from the original papers when available; otherwise, we reproduce them. Note that EM-Diffusion requires 50 clean samples for initialization, whereas our method is trained entirely without access to clean data. Underscored values refer to the teacher models of RSD for each task. RSD consistently outperforms the teacher models, even surpassing EM-Diffusion (few-shot) in all settings except for Gaussian deblurring at $\sigma = 0.2$.

Methods	σ	Gaussian Deblurring	Random Inpainting ($p = 0.9$)	Super-Resolution ($\times 2$)
Observation	0.0	72.83	396.14	23.94
Standard Diffusion		<u>94.40</u>	-	<u>23.28</u>
Ambient Diffusion		-	<u>25.53</u>	-
EM-Diffusion (<i>Few-Shot</i>)		56.69	104.68	58.99
RSD (ours, one-step)		31.90	16.86	12.99
Observation	0.2	264.37	419.92	200.04
Ambient Tweedie		<u>99.19</u>	<u>319.34</u>	<u>23.92</u>
EM-Diffusion (<i>Few-Shot</i>)		51.33	165.60	57.31
RSD (ours, one-step)		76.98	79.48	22.00

Table 3: **Results of our method RSD on CelebA-HQ w.r.t Random Inpainting across different missing rate p .** Note that our results are directly obtained by distilling from publicly available checkpoints released by Ambient Diffusion.

Method	Type	$p = 0.6$	$p = 0.8$	$p = 0.9$
Observation		275.04	383.82	396.14
Ambient Diffusion	Teacher	6.08	11.19	25.53
RSD (ours, one-step)	Distilled	4.44	7.10	16.86

use truncated sampling by default to achieve better performance. 3) **Ambient Diffusion** [9] (Appendix E.3): Ambient Diffusion improves learning from masked data (i.e., inpainting) by introducing an additional measurement mask during the diffusion process and training the model to reconstruct the original masked image from a more heavily corrupted input. To demonstrate the flexibility of our distillation method, we directly distill from the publicly released Ambient Diffusion checkpoint for the random inpainting task. 4) **EM-Diffusion (Few-Shot)** [3]: EM-Diffusion takes a different approach by alternating between two steps. First, it reconstructs clean images from corrupted data using a known but low-quality diffusion model via DPS [7] (E-step). Then, it refines the model weights based on these reconstructions (M-step). These steps are repeated iteratively to progressively learn a diffusion model for the clean data distribution. Note that an additional 50 clean images are required to initialize EM-Diffusion training. In this context, we refer to it as a few-shot initialization. Our implementation shows that even using a small number of clean images for initialization can lead to a reasonably good FID (e.g., FID 56.15 at initialization). This further highlights the strength of our approach, which achieves competitive performance while being entirely free from clean data.

Diverse restoration tasks. We evaluate our method on three representative image restoration tasks: (1) **Gaussian deblurring**, using a Gaussian blur kernel of size 9×9 with a standard deviation $\sigma_G = 2$ pixels; (2) **random inpainting**, with a missing rate of $p = 0.9$; and (3) **super-resolution**, with a downsampling factor of $\times 2$. All tasks are evaluated under both noisy and noiseless corruption settings. As shown in Tab. 2, our method consistently outperforms the corresponding teacher diffusion models (i.e., underscored values in the table) across all tasks and corruption regimes. For the random inpainting task, we use Ambient Diffusion to implement the teacher models. Notably, RSD also surpasses EM-Diffusion, a baseline that leverages few-shot supervision via clean initialization, in all settings except Gaussian deblurring at $\sigma = 0.2$. These results highlight the effectiveness of our fully unsupervised approach. Qualitative comparisons demonstrating the visual fidelity of our method are provided in Fig. 1, Appendix A, and Appendix H.

Distilling from existing diffusion checkpoints. Tab. 2 demonstrates that our framework RSD is compatible with various pretraining objectives including Standard Diffusion, Ambient Tweedie, and Ambient Diffusion. To further demonstrate the generality and flexibility of our framework, we distill all the publicly released Ambient Diffusion checkpoints for the random inpainting task at missing rate

Table 4: **FID scores across varying acceleration levels R in the multi-coil MRI setting.** Our method consistently outperforms both the teacher model and L1-EDM, which is trained on L1-Wavelet reconstructions of corrupted samples. Note that our results are directly obtained by distilling from publicly available checkpoints released by Fourier-Space Ambient Diffusion.

Method	Type	$R = 2$	$R = 4$	$R = 6$	$R = 8$
L1-EDM		18.5534	27.6405	51.4272	102.984
Fourier-Space Ambient Diffusion	Teacher	30.3425	32.3101	31.5033	48.1525
RSD (ours, one-step)	Distilled	12.9450	10.7119	14.6410	22.5100

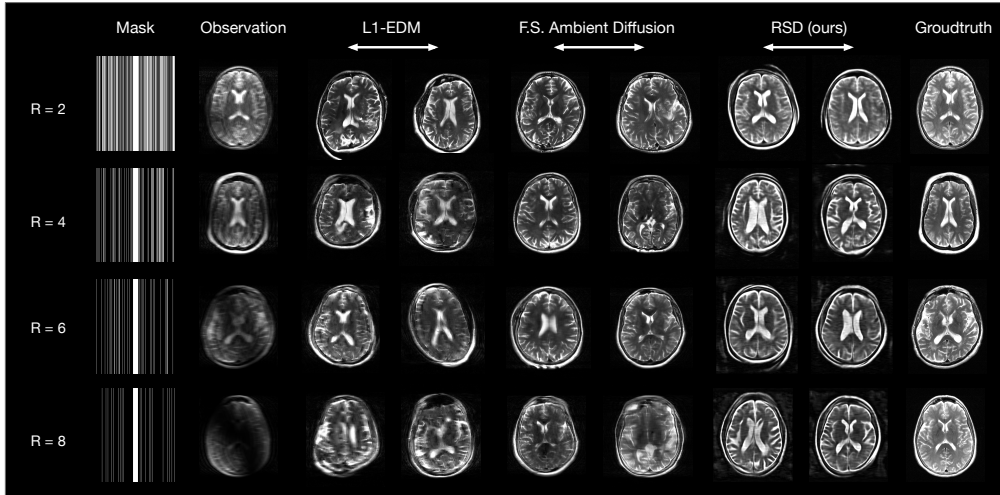


Figure 3: **Qualitative results of our method RSD on multi-coil MRI.**

$p \in \{0.6, 0.8, 0.9\}$. Results in Tab. 3 show that even under severe occlusion with high missing rates, our distilled model significantly improves upon the original Ambient Diffusion teacher, confirming the robustness of our approach across different corruption intensities and teacher sources.

5.2 Multi-Coil Magnetic Resonance Imaging (MRI)

In this section, we: 1) apply our RSD framework to a practical medical imaging problem, i.e., multi-coil MRI where fully sampled images are often unavailable due to the time and cost [21, 47, 39, 12]; 2) demonstrate the flexibility of RSD by distilling from diffusion checkpoints pretrained on corrupted data released by [2], proving again that our method can be seamlessly integrated with existing advanced corruption-aware diffusion techniques; and 3) extend our RSD framework from the real to the complex domain, i.e., $x \in \mathbb{C}^d$.

In the multi-coil MRI setting, image acquisition involves collecting measurements directly in the spatial frequency domain from a set of spatially localized coils. Suppose there are N_c coils. Following [2], each measurement is given by $y = (\sum_{i=1}^{N_c} S_i^H \mathcal{F}^{-1} M \mathcal{F} S_i) x$, where S_i denotes the coil sensitivity profile of the i -th coil, \mathcal{F} is the Fourier transform, and M is the masking operator in Fourier space. The number of measurements m depends on the subsampling operator P . We define the acceleration level as $R = \frac{d}{m}$, which quantifies the degree of subsampling. An acceleration rate of $R = 1$ corresponds to a fully supervised setting, while larger values of R indicate higher levels of corruption and subsampling.

Tab. 4 presents FID comparisons between our method (RSD), Fourier-Space Ambient Diffusion [2], and L1-EDM [20, 25] across acceleration factors $R \in \{2, 4, 6, 8\}$. Qualitative samples are presented in Fig. 3. Similar to Ambient Diffusion [9], Aali et al. [2] enhances diffusion training on corrupted MRI data by further corruption with additional \tilde{M} , serving as the pretrained teacher model for RSD. L1-EDM refers to EDM [20] models trained on L1-Wavelet compressed sensing reconstructions of the training data at each acceleration level [25]. RSD consistently outperforms the teacher model across all acceleration rates, highlighting the strength of our framework. Notably, RSD also surpasses L1-EDM at low acceleration ($R = 2$), suggesting that score distillation provides more effective

regularization than handcrafted L1 priors in the wavelet domain. A full description of our algorithm is provided in Appendix E.4 and Appendix F.

5.3 Proximal FID as a Model Selection Metric

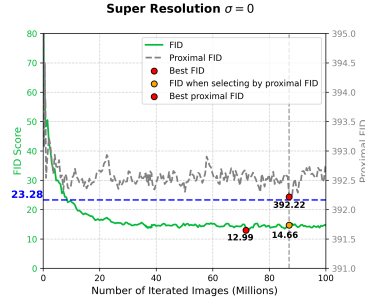


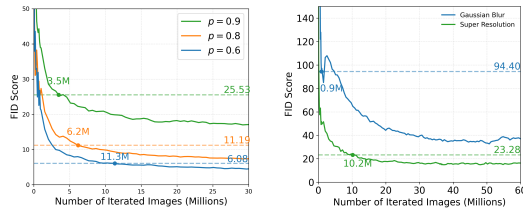
Figure 4: Proximal FID for model selection in the Super-Resolution task with $\sigma = 0$.

As illustrated in Fig. 4, selecting models based on the proximal FID yields a score of 14.66—only 1.67 points higher than the best possible true FID achieved during training. This demonstrates that proximal FID is an effective proxy for standard FID when clean images are unavailable. Additional model selection results are provided in Appendix G.4 and Tab. 6.

In scenarios where only corrupted data is available, it is crucial to develop a reliable method for selecting the model that achieves optimal performance. In standard image generation tasks, FID is widely used to identify the model that yields the highest image quality. However, since clean data is not available in our setting, computing FID against clean ground-truth images is infeasible.

Previous baseline approaches—such as Ambient Diffusion [8] and EM-Diffusion [3]—report FID scores but do not address how to perform model selection during training. To this end, we propose a new metric, Proximal FID, extending the model selection strategy introduced in DSD [6]. Specifically, we compute the FID between the set $\{\mathcal{A}(x^{(i)}) + \sigma\epsilon\}_{i=1}^{50k}$ and the corrupted dataset $\{y^{(i)}\}_{i=1}^n$, where $x^{(i)}$ denotes the clean image

5.4 Data Efficiency for Distillation



(a) Random inpainting with varying probabilities. (b) Gaussian Deblurring and Super-Resolution.

Figure 5: FID curves during the distillation process. The horizontal line indicates the FID achieved by the teacher diffusion model.

Moreover, our method reduces the generation process to a single step and continues to improve image quality with further training.

Unlike previous baseline methods, we propose the first distillation framework capable of addressing general inverse problems in an unsupervised setting. A natural concern is whether this approach demands substantial additional effort beyond pretraining a diffusion model. It is worth noting that training a high-quality diffusion model typically requires approximately 100 million image iterations (see EDM [20]). In contrast, we show that our distillation method is significantly data-efficient across various tasks (see Fig. 5). As shown in the results across five different tasks, our framework requires no more than 12 million image iterations to surpass the performance of the teacher diffusion model.

6 Conclusion

In this work, we introduced Restoration Score Distillation (RSD) to learn from a broad class of corruption types. Our empirical results on natural images and scientific MRI datasets show consistent improvements over existing baselines. Moreover, beyond standard diffusion objectives, the RSD framework is compatible with several corruption-aware training techniques such as Ambient Tweedie, Ambient Diffusion, and its Fourier-space variant, enabling flexible integration with recent advances in diffusion modeling. Theoretical analysis further reveals that RSD implicitly aligns the generator with the eigenspace of the clean data distribution, providing a principled understanding of its regularization benefits. Together, our contributions highlight the potential of score distillation as a powerful mechanism for robust generative learning in real-world settings where clean data are scarce or unavailable. A detailed discussion of limitations is provided in Appendix B.

References

- [1] Maximum likelihood from incomplete data via the em algorithm. *Journal of the royal statistical society: series B (methodological)*, 39(1):1–22, 1977.
- [2] A. Aali, G. Daras, B. Levac, S. Kumar, A. Dimakis, and J. Tamir. Ambient diffusion posterior sampling: Solving inverse problems with diffusion models trained on corrupted data. In *The Thirteenth International Conference on Learning Representations*, 2025. URL <https://openreview.net/forum?id=qeXcMutEZY>.
- [3] W. Bai, Y. Wang, W. Chen, and H. Sun. An expectation-maximization algorithm for training clean diffusion models from corrupted observations. In *The Thirty-eighth Annual Conference on Neural Information Processing Systems*, 2024. URL <https://openreview.net/forum?id=jURBh4V9N4>.
- [4] Y. Chang, Y. Zhang, Z. Fang, Y. N. Wu, Y. Bisk, and F. Gao. Skews in the phenomenon space hinder generalization in text-to-image generation. In A. Leonardis, E. Ricci, S. Roth, O. Russakovsky, T. Sattler, and G. Varol, editors, *Computer Vision – ECCV 2024*, pages 422–439, Cham, 2025. Springer Nature Switzerland. ISBN 978-3-031-73021-4.
- [5] T. Chen, Z. Wang, and M. Zhou. Enhancing and accelerating diffusion-based inverse problem solving through measurements optimization. *arXiv preprint arXiv:2412.03941*, 2024.
- [6] T. Chen, Y. Zhang, Z. Wang, Y. N. Wu, O. Leong, and M. Zhou. Denoising score distillation: From noisy diffusion pretraining to one-step high-quality generation. *arXiv preprint arXiv:2503.07578*, 2025.
- [7] H. Chung, J. Kim, M. T. Mccann, M. L. Klasky, and J. C. Ye. Diffusion posterior sampling for general noisy inverse problems. *arXiv preprint arXiv:2209.14687*, 2022.
- [8] G. Daras, K. Shah, Y. Dagan, A. Gollakota, A. Dimakis, and A. Klivans. Ambient diffusion: Learning clean distributions from corrupted data. *Advances in Neural Information Processing Systems*, 36:288–313, 2023.
- [9] G. Daras, K. Shah, Y. Dagan, A. Gollakota, A. Dimakis, and A. Klivans. Ambient diffusion: Learning clean distributions from corrupted data. *Advances in Neural Information Processing Systems*, 36:288–313, 2023.
- [10] G. Daras, A. Dimakis, and C. C. Daskalakis. Consistent diffusion meets tweedie: Training exact ambient diffusion models with noisy data. In *Forty-first International Conference on Machine Learning*, 2024. URL <https://openreview.net/forum?id=PlVjIGaFdh>.
- [11] G. Daras, Y. Cherapanamjeri, and C. C. Daskalakis. How much is a noisy image worth? data scaling laws for ambient diffusion. In *The Thirteenth International Conference on Learning Representations*, 2025. URL <https://openreview.net/forum?id=qZwtPEw2qN>.
- [12] A. D. Desai, A. M. Schmidt, E. B. Rubin, C. M. Sandino, M. S. Black, V. Mazzoli, K. J. Stevens, R. Boutin, C. Ré, G. E. Gold, et al. Skm-tea: A dataset for accelerated mri reconstruction with dense image labels for quantitative clinical evaluation. *arXiv preprint arXiv:2203.06823*, 2022.
- [13] P. Dhariwal and A. Nichol. Diffusion models beat gans on image synthesis. *Advances in neural information processing systems*, 34:8780–8794, 2021.
- [14] M. Heusel, H. Ramsauer, T. Unterthiner, B. Nessler, and S. Hochreiter. Gans trained by a two time-scale update rule converge to a local nash equilibrium. *Advances in neural information processing systems*, 30, 2017.
- [15] N. J. Higham. *Accuracy and stability of numerical algorithms*. SIAM, 2002.
- [16] J. Ho, A. Jain, and P. Abbeel. Denoising diffusion probabilistic models. *Advances in neural information processing systems*, 33:6840–6851, 2020.
- [17] J. Ho, C. Saharia, W. Chan, D. J. Fleet, M. Norouzi, and T. Salimans. Cascaded diffusion models for high fidelity image generation. *Journal of Machine Learning Research*, 23(47):1–33, 2022.
- [18] A. Jalal, M. Arvinte, G. Daras, E. Price, A. G. Dimakis, and J. Tamir. Robust compressed sensing mri with deep generative priors. *Advances in Neural Information Processing Systems*, 34:14938–14954, 2021.
- [19] T. Karras, T. Aila, S. Laine, and J. Lehtinen. Progressive growing of gans for improved quality, stability, and variation. *arXiv preprint arXiv:1710.10196*, 2017.

- [20] T. Karras, M. Aittala, T. Aila, and S. Laine. Elucidating the design space of diffusion-based generative models. *Advances in neural information processing systems*, 35:26565–26577, 2022.
- [21] F. Knoll, J. Zbontar, A. Sriram, M. J. Muckley, M. Bruno, A. Defazio, M. Parente, K. J. Geras, J. Katsnelson, H. Chandarana, et al. fastmri: A publicly available raw k-space and dicom dataset of knee images for accelerated mr image reconstruction using machine learning. *Radiology: Artificial Intelligence*, 2(1): e190007, 2020.
- [22] Y. Y. Lin, A. F. Gao, and K. L. Bouman. Imaging an evolving black hole by leveraging shared structure. In *ICASSP 2024-2024 IEEE International Conference on Acoustics, Speech and Signal Processing (ICASSP)*, pages 2475–2479. IEEE, 2024.
- [23] Z. Liu, P. Luo, X. Wang, and X. Tang. Deep learning face attributes in the wild. In *Proceedings of the IEEE international conference on computer vision*, pages 3730–3738, 2015.
- [24] W. Luo, T. Hu, S. Zhang, J. Sun, Z. Li, and Z. Zhang. Diff-instruct: A universal approach for transferring knowledge from pre-trained diffusion models. *Advances in Neural Information Processing Systems*, 36, 2024.
- [25] M. Lustig, D. Donoho, and J. M. Pauly. Sparse mri: The application of compressed sensing for rapid mr imaging. *Magnetic Resonance in Medicine: An Official Journal of the International Society for Magnetic Resonance in Medicine*, 58(6):1182–1195, 2007.
- [26] G. Nolet. A breviary of seismic tomography. *A breviary of seismic tomography*, 2008.
- [27] W. Peebles and S. Xie. Scalable diffusion models with transformers. In *Proceedings of the IEEE/CVF International Conference on Computer Vision*, pages 4195–4205, 2023.
- [28] B. Poole, A. Jain, J. T. Barron, and B. Mildenhall. Dreamfusion: Text-to-3d using 2d diffusion. *arXiv preprint arXiv:2209.14988*, 2022.
- [29] A. Ramesh, P. Dhariwal, A. Nichol, C. Chu, and M. Chen. Hierarchical text-conditional image generation with clip latents. *arXiv preprint arXiv:2204.06125*, 1(2):3, 2022.
- [30] N. Rawlinson, A. Fichtner, M. Sambridge, and M. K. Young. Seismic tomography and the assessment of uncertainty. *Advances in geophysics*, 55:1–76, 2014.
- [31] A. W. Reed, H. Kim, R. Anirudh, K. A. Mohan, K. Champley, J. Kang, and S. Jayasuriya. Dynamic ct reconstruction from limited views with implicit neural representations and parametric motion fields. In *Proceedings of the IEEE/CVF International Conference on Computer Vision*, pages 2258–2268, 2021.
- [32] F. Roddier. Interferometric imaging in optical astronomy. *Physics Reports*, 170(2):97–166, 1988.
- [33] R. Rombach, A. Blattmann, D. Lorenz, P. Esser, and B. Ommer. High-resolution image synthesis with latent diffusion models. In *Proceedings of the IEEE/CVF conference on computer vision and pattern recognition*, pages 10684–10695, 2022.
- [34] O. Ronneberger, P. Fischer, and T. Brox. U-net: Convolutional networks for biomedical image segmentation. In *Medical image computing and computer-assisted intervention–MICCAI 2015: 18th international conference, Munich, Germany, October 5-9, 2015, proceedings, part III 18*, pages 234–241. Springer, 2015.
- [35] C. Saharia, W. Chan, S. Saxena, L. Li, J. Whang, E. L. Denton, K. Ghasemipour, R. Gontijo Lopes, B. Karagol Ayan, T. Salimans, et al. Photorealistic text-to-image diffusion models with deep language understanding. *Advances in neural information processing systems*, 35:36479–36494, 2022.
- [36] J. Sohl-Dickstein, E. Weiss, N. Maheswaranathan, and S. Ganguli. Deep unsupervised learning using nonequilibrium thermodynamics. In *International conference on machine learning*, pages 2256–2265. PMLR, 2015.
- [37] Y. Song and S. Ermon. Generative modeling by estimating gradients of the data distribution. *Advances in neural information processing systems*, 32, 2019.
- [38] Y. Song, J. Sohl-Dickstein, D. P. Kingma, A. Kumar, S. Ermon, and B. Poole. Score-based generative modeling through stochastic differential equations. In *International Conference on Learning Representations*, 2021. URL <https://openreview.net/forum?id=PxtTIG12RRHS>.
- [39] R. Tibrewala, T. Dutt, A. Tong, L. Ginocchio, M. B. Keerthivasan, S. H. Baete, S. Chopra, Y. W. Lui, D. K. Sodickson, H. Chandarana, et al. Fastmri prostate: A publicly available, biparametric mri dataset to advance machine learning for prostate cancer imaging. *arXiv preprint arXiv:2304.09254*, 2023.

- [40] M. Uecker, P. Lai, M. J. Murphy, P. Virtue, M. Elad, J. M. Pauly, S. S. Vasanawala, and M. Lustig. Espirit—an eigenvalue approach to autocalibrating parallel mri: where sense meets grappa. *Magnetic resonance in medicine*, 71(3):990–1001, 2014.
- [41] P. Vincent. A connection between score matching and denoising autoencoders. *Neural computation*, 23(7): 1661–1674, 2011.
- [42] Z. Wang, C. Lu, Y. Wang, F. Bao, C. Li, H. Su, and J. Zhu. Prolificdreamer: High-fidelity and diverse text-to-3d generation with variational score distillation. *Advances in Neural Information Processing Systems*, 36, 2024.
- [43] S. Xie, Z. Xiao, D. P. Kingma, T. Hou, Y. N. Wu, K. P. Murphy, T. Salimans, B. Poole, and R. Gao. EM distillation for one-step diffusion models. In *The Thirty-eighth Annual Conference on Neural Information Processing Systems*, 2024. URL <https://openreview.net/forum?id=rafVvthuxD>.
- [44] Y. Xu, W. Nie, and A. Vahdat. One-step diffusion models with f -divergence distribution matching. *arXiv preprint arXiv:2502.15681*, 2025.
- [45] T. Yin, M. Gharbi, T. Park, R. Zhang, E. Shechtman, F. Durand, and B. Freeman. Improved distribution matching distillation for fast image synthesis. *Advances in neural information processing systems*, 37: 47455–47487, 2024.
- [46] T. Yin, M. Gharbi, R. Zhang, E. Shechtman, F. Durand, W. T. Freeman, and T. Park. One-step diffusion with distribution matching distillation. In *Proceedings of the IEEE/CVF Conference on Computer Vision and Pattern Recognition*, pages 6613–6623, 2024.
- [47] J. Zbontar, F. Knoll, A. Sriram, T. Murrell, Z. Huang, M. J. Muckley, A. Defazio, R. Stern, P. Johnson, M. Bruno, et al. fastmri: An open dataset and benchmarks for accelerated mri. *arXiv preprint arXiv:1811.08839*, 2018.
- [48] Y. Zhang and O. Leong. Learning difference-of-convex regularizers for inverse problems: A flexible framework with theoretical guarantees. *arXiv preprint arXiv:2502.00240*, 2025.
- [49] Y. Zhang, P. Yu, Y. Zhu, Y. Chang, F. Gao, Y. N. Wu, and O. Leong. Flow priors for linear inverse problems via iterative corrupted trajectory matching. In *The Thirty-eighth Annual Conference on Neural Information Processing Systems*, 2024. URL <https://openreview.net/forum?id=1H2e7USI09>.
- [50] Y. Zhang, P. Yu, and Y. N. Wu. Object-conditioned energy-based attention map alignment in text-to-image diffusion models. In A. Leonardis, E. Ricci, S. Roth, O. Russakovsky, T. Sattler, and G. Varol, editors, *Computer Vision – ECCV 2024*, pages 55–71, Cham, 2025. Springer Nature Switzerland. ISBN 978-3-031-72946-1.
- [51] H. Zheng, Z. Wang, J. Yuan, G. Ning, P. He, Q. You, H. Yang, and M. Zhou. Learning stackable and skippable LEGO bricks for efficient, reconfigurable, and variable-resolution diffusion modeling. In *The Twelfth International Conference on Learning Representations*, 2024. URL <https://openreview.net/forum?id=qmXedvwrT1>.
- [52] M. Zhou, H. Zheng, Z. Wang, M. Yin, and H. Huang. Score identity distillation: Exponentially fast distillation of pretrained diffusion models for one-step generation. In *Forty-first International Conference on Machine Learning*, 2024.
- [53] Y. Zhu, Z. Dou, H. Zheng, Y. Zhang, Y. N. Wu, and R. Gao. Think twice before you act: Improving inverse problem solving with mcmc. *arXiv preprint arXiv:2409.08551*, 2024.

Appendix

A Qualitative Snapshots of Generated Results

In this section, we present visual examples highlighting the quality of outputs produced by our model across various tasks and corruption settings.

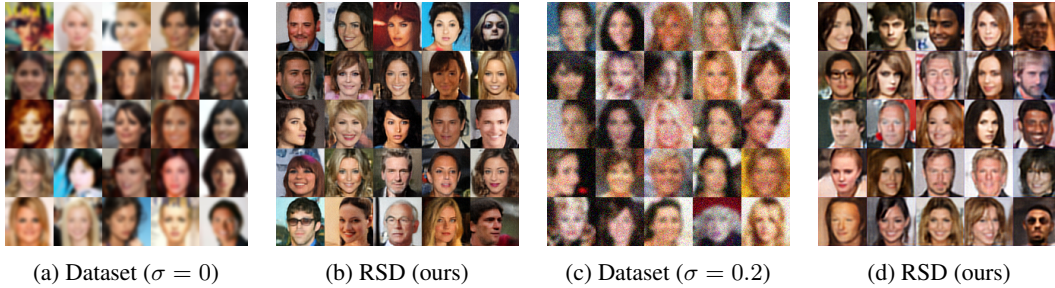


Figure 6: Qualitative results for the Gaussian blur task. Each pair shows the corrupted input and the generation output from our RSD.

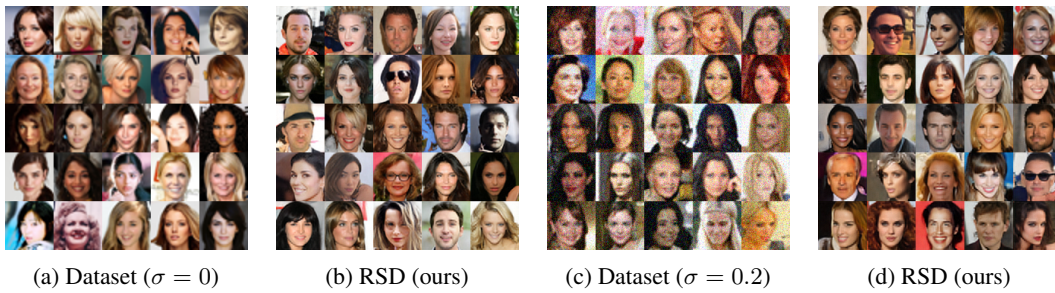


Figure 7: Qualitative results for the Super Resolution task. Each pair shows the corrupted input and the generation output from our RSD.

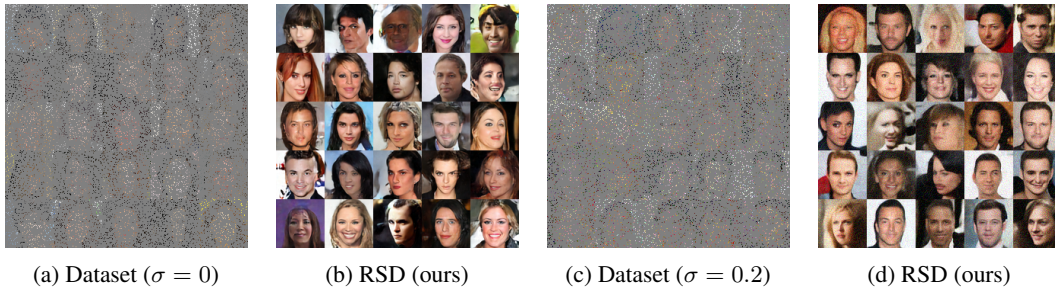


Figure 8: Qualitative results for the Random Inpainting task with missing probability ($p = 0.9$). Each pair shows the corrupted input and the generation output from our RSD.

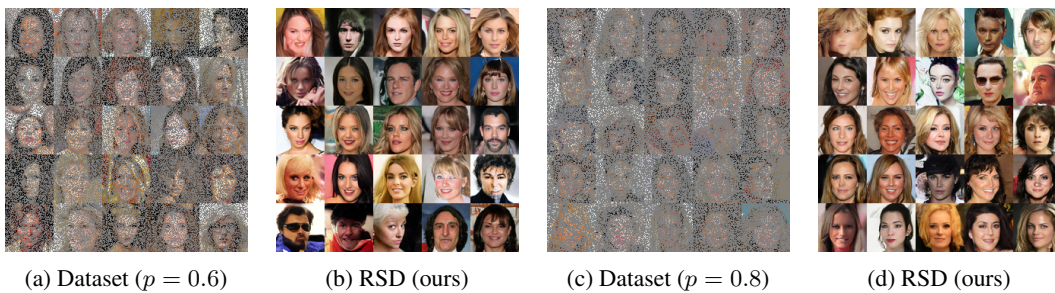


Figure 9: Qualitative results for the Random Inpainting task with different missing probability ($p = 0.6, p = 0.8$). Each pair shows the corrupted input and the generation output from our RSD.

B Discussions and Limitations

Unknown corruption operator. In practical scenarios where only corrupted datasets are available, the true corruption operator is often unknown. Note that in our method, we do not require the exact formulas for the operator. Instead we only have access to the propagation results of the corruption process. This highlights a significant advantage of our approach: the ability to infer properties of the underlying data distribution without explicit knowledge of how the corruption has occurred.

Solving inverse problems. While our method effectively learns a clean data distribution from corrupted observations, it does not inherently support conditional sampling based on a specific observation. A promising future direction is to extend our framework into a conditional solver for inverse problems [7, 49, 53, 48, 5], enabling applications in scientific and engineering domains where recovering corresponding clean samples from measurements is critical.

Applications in scientific discovery. Our proposed approach is particularly well-suited for scientific discovery applications, where access to clean observational data is inherently limited. Applying our method to other datasets across different scientific domains is a promising avenue for future research.

C Comparison with Denoising Score Distillation

We highlight the differences between our RSD framework and DSD [6] in the following aspects:

1. DSD primarily focuses on standard diffusion and ambient Tweedie in the pure noise setting, i.e., $x + \sigma\epsilon$, where \mathcal{A} reduces to the identity matrix. In contrast, our RSD framework extends DSD to handle a general corruption operator \mathcal{A} , with adaptation in both the pretraining and distillation stages.
2. RSD also explores and enhances other advanced corruption-aware diffusion techniques, including Ambient Diffusion and Fourier-Space Ambient Diffusion. This makes our framework flexible across different objectives and applicable in both image and Fourier domains, allowing us to tackle corrupted data in both natural and scientific settings.
3. The theory here generalizes that of DSD by allowing for general linear corruption operators \mathcal{A} acting on the data along with additive Gaussian noise.

D Proof of Theorem 1

We first record auxilliary results that will aid in establishing Theorem 1.

Lemma 1. [Generalized Woodbury Matrix Identity [15]]

Given an invertible square matrix $A \in \mathbb{R}^{n \times n}$, along with matrices $U \in \mathbb{R}^{n \times k}$ and $V \in \mathbb{R}^{k \times n}$, define the perturbed matrix: $B = A + UV$. If $(I_k + VA^{-1}U)$ is invertible, then the inverse of B is given by:

$$B^{-1} = A^{-1} - A^{-1}U(I_k + VA^{-1}U)^{-1}VA^{-1}.$$

First, we show that the objective under the parameterization $\theta = (u, u/\|u\|)$ simplifies into a form that we directly analyze.

Lemma 2. Consider the setting of Theorem 1. For $t \in [0, 1]$, let $a_t := \sigma_t^2$, $c_t := a_t + \sigma^2$, and $\eta_t := \frac{2c_t + \|Ae\|^2}{c_t^2(c_t + \|Ae\|^2)}$. Then the objective $\mathcal{L}(\theta)$ with $\theta = (u, u/\|u\|)$ satisfies the following: there exists a constant C independent of $u \in \mathbb{R}^d$ such that

$$\mathcal{L}(\theta) = C + L(u)$$

where

$$L(u) := \mathbb{E}_{t \sim \text{Unif}[0,1]} \left[\frac{1}{c_t^2} \|Au\|^2 - \eta_t (e^T A^T Au)^2 - \frac{\|Au\|^2}{a_t(a_t + \|Au\|^2)} \right].$$

Proof of Lemma 2. Consider the loss function $\mathcal{L}(\theta)$ under the parameterization $\theta = (u, u/\|u\|)$ for $u \neq 0$:

$$\mathcal{L}(\theta) := \mathbb{E}_{t \sim \text{Unif}[0,1]} \mathbb{E}_{y_t \sim \tilde{p}_{G\theta}^{\sigma_t}} \left[\left\| \left(\Sigma_{t,e,A}^{-1} - \Sigma_{t,\theta,A} \right)^{-1} y_t \right\|_2^2 \right]$$

where

$$\Sigma_{t,e,A} := Aee^T A^T + c_t I_m \text{ and } \Sigma_{t,\theta,A} := Auu^T A^T + a_t I_m.$$

Using a similar reduction in [6], we get that the above loss equals

$$\mathcal{L}(\theta) = \mathbb{E}_{t \sim \text{Unif}[0,1]} [C_{\sigma,t}] + \mathbb{E}_{t \sim \text{Unif}[0,1]} \left[\text{tr} \left(\Sigma_{t,e,A}^{-2} \Sigma_{t,\theta,A} \right) \right] + \mathbb{E}_{t \sim \text{Unif}[0,1]} \left[\text{tr} \left(\Sigma_{t,\theta,A}^{-1} \right) \right]$$

where $C_{\sigma,t}$ is a constant that depends only on time and σ and not on θ . Note that Using the Woodbury matrix identity in Lemma 1, we get

$$\Sigma_{t,e,A}^{-2} = (Aee^T A^T + c_t I_m)^{-2} = c_t^{-2} I_m - \frac{2c_t + \|Ae\|^2}{c_t^2(c_t + \|Ae\|^2)} Aee^T A^T$$

which implies

$$\begin{aligned} \Sigma_{t,e,A}^{-2} \Sigma_{t,\theta,A} &= \left(c_t^{-2} I_m - \frac{2c_t + \|Ae\|^2}{c_t^2(c_t + \|Ae\|^2)} Aee^T A^T \right) Auu^T A^T \\ &\quad + c_t^{-2} a_t I_m - a_t \frac{2c_t + \|Ae\|^2}{c_t^2(c_t + \|Ae\|^2)} Aee^T A^T \\ &= c_t^{-2} Auu^T A^T - \eta_t Aee^T A^T Auu^T A^T + c_t^{-2} a_t I_m - a_t \eta_t Aee^T A^T. \end{aligned}$$

Also, we have that

$$\Sigma_{t,\theta,A}^{-1} = (Auu^T A^T + a_t I_m)^{-1} = a_t^{-1} I_m - \frac{Auu^T A^T}{a_t(a_t + \|Au\|^2)}.$$

Thus computing the trace, taking an expectation, and collecting terms that only involve u , we see that there exists a constant C depending on (σ_t) , σ , A , and e (independent of u) such that

$$\begin{aligned} \mathcal{L}(\theta) &= C + \mathbb{E}_t [c_t^{-2}] \text{tr}(Auu^T A^T) - \mathbb{E}_t [\eta_t] \text{tr}(Aee^T A^T Auu^T A^T) - \mathbb{E}_t \left[\frac{\text{tr}(Auu^T A^T)}{a_t(a_t + \|Au\|^2)} \right] \\ &= C + \mathbb{E}_t [c_t^{-2}] \|Au\|^2 - \mathbb{E}_t [\eta_t] (e^T A^T Au)^2 - \mathbb{E}_t \left[\frac{\|Au\|^2}{a_t(a_t + \|Au\|^2)} \right] \\ &=: C + L(u). \end{aligned}$$

□

Proof of Theorem 1. Note that Lemma 2 shows that we have the simpler formula

$$\mathcal{L}(\theta) = C + L(u)$$

where

$$L(u) := \mathbb{E}_t \left[\frac{1}{c_t^2} \|Au\|^2 - \eta_t (e^T A^T Au)^2 - \frac{\|Au\|^2}{a_t(a_t + \|Au\|^2)} \right]$$

For notational simplicity, let $G = A^T A$, $g(u) = u^T G u$, $h(u) = e^T G u$, $\phi_t(g) = g/(a_t(a_t + g))$, and $\eta_t := (2c_t + \|Ae\|^2)/(c_t^2(c_t + \|Ae\|^2)^2)$. Then our objective results in

$$L(u) := \mathbb{E}_t [c_t^{-2}] g(u) - \mathbb{E}_t [\eta_t] h(u)^2 - \mathbb{E}_t [\phi_t(g(u))] =: \tilde{c}g(u) - \tilde{\eta}h(u)^2 - \mathbb{E}_t [\phi_t(g(u))].$$

We claim that any global minimizer of L is of the form $u_* = \pm \lambda_* e + q$ for some constant λ_* to be defined and $q \in \ker(A)$. First, note that we can lower bound $L(u)$ by another function $\Psi(g(u))$ as follows: since G is PSD, note that we have the generalized Cauchy Schwarz inequality:

$$h(u)^2 = (e^T G u)^2 \leq (e^T G e)(u^T G u) = g(e)g(u).$$

Moreover, this holds with equality if and only if Au and Ae are collinear, i.e., $Au = \lambda Ae$ or equivalently $u = \lambda e + v$ for $v \in \ker(A)$. Then we get the lower bound

$$L(u) = \tilde{c}g(u) - \tilde{\eta}h(u)^2 - \mathbb{E}_t [\phi_t(g(u))] \geq (\tilde{c} - \tilde{\eta}\|Ae\|^2)g(u) - \mathbb{E}_t [\phi_t(g(u))] =: \Psi(g(u))$$

where we have defined the new function $\Psi(g) := (\tilde{c} - \tilde{\eta}\|Ae\|^2)g - \mathbb{E}_t[\phi_t(g)]$ for $g \geq 0$. Since $g(u) \geq 0$ for every u , we have that

$$L(u) \geq \min_{g \geq 0} \Psi(g).$$

We first analyze the minimizers of Ψ and then construct u_* such that $L(u_*) = \Psi(g_*)$. First let $\Delta = (\tilde{c} - \tilde{\eta}\|Ae\|^2)$ which is given by

$$\Delta = \mathbb{E}_t [c_t^{-2} - \eta_t \|Ae\|^2] = \mathbb{E}_t \left[\frac{1}{c_t^2} - \frac{(2c_t + \|Ae\|^2)\|Ae\|^2}{c_t^2(c_t + \|Ae\|^2)^2} \right].$$

We claim that $\Delta > 0$. Indeed, note that for any $g > 0$,

$$\begin{aligned} \frac{g(2c_t + g)}{(c_t + g)^2} &= \frac{g(2c_t + g)g}{c_t^2 + (2c_t + g)g} \\ &= \frac{g(2c_t + g) + c_t^2 - c_t^2}{c_t^2 + (2c_t + g)g} \\ &= 1 - \frac{c_t^2}{(c_t + g)^2}. \end{aligned}$$

Applying this to Δ with $g = \|Ae\|^2$ yields

$$\begin{aligned} \Delta &= \mathbb{E}_t \left[\frac{1}{c_t^2} - \frac{(2c_t + \|Ae\|^2)\|Ae\|^2}{c_t^2(c_t + \|Ae\|^2)^2} \right] \\ &= \mathbb{E}_t \left[\frac{1}{c_t^2} \left(1 - \frac{(2c_t + \|Ae\|^2)\|Ae\|^2}{(c_t + \|Ae\|^2)^2} \right) \right] \\ &= \mathbb{E}_t \left[\frac{1}{c_t^2} \left(1 - 1 + \frac{c_t^2}{(c_t + \|Ae\|^2)^2} \right) \right] \\ &= \mathbb{E}_t \left[\frac{1}{(c_t + \|Ae\|^2)^2} \right] > 0 \end{aligned}$$

as desired. This gives

$$\Psi(g) = \Delta g - \mathbb{E}_t[\phi_t(g)].$$

Observe that

$$\Psi'(g) = \Delta - \frac{\partial}{\partial g} \int_0^1 \frac{g}{a_t^2 + a_t g} dt = \Delta - \int_0^1 \frac{a_t^2}{(a_t^2 + a_t g)^2} dt = \Delta - \mathbb{E}_t \left[\frac{1}{(a_t + g)^2} \right]$$

and

$$\Psi''(g) = -\partial/\partial g \mathbb{E}_t[(a_t + g)^{-2}] = 2\mathbb{E}_t[(a_t + g)^{-3}] > 0 \quad \forall g.$$

Hence the function Ψ is strictly convex. Moreover, a sign analysis reveals that

$$\Psi'(0) = \Delta - \mathbb{E}_t[1/a_t^2] = \mathbb{E}_t \left[\frac{1}{(c_t + \|Ae\|^2)^2} - \frac{1}{a_t^2} \right] = \mathbb{E}_t \left[\frac{1}{(\sigma^2 + a_t + \|Ae\|^2)^2} - \frac{1}{a_t^2} \right] < 0$$

while for $g > \sigma^2 + \|Ae\|^2$, we have

$$\Psi'(g) = \mathbb{E}_t \left[\frac{1}{(\sigma^2 + a_t + \|Ae\|^2)^2} - \frac{1}{(a_t + g)^2} \right] > 0$$

so there must exist a unique root g_* such that $\Psi'(g_*) = 0$. In fact, $g_* = \sigma^2 + \|Ae\|^2$ achieves $\Psi'(g_*) = 0$. Finally, we have that

$$L(u) \geq \min_{g \geq 0} \Psi(g) = \Psi(g_*) = \Delta(\sigma^2 + \|Ae\|^2) - \mathbb{E}_t[\phi_t(\sigma^2 + \|Ae\|^2)].$$

We claim that $u_* = \pm \sqrt{g_*/\|Ae\|^2}e$ achieves $L(u_*) = \Psi(g_*)$. Indeed, note that $g(u_*) = (u_*)^T G u_* = g_*/\|Ae\|^2 e^T G e = g_*/\|Ae\|^2 \cdot \|Ae\|^2 = g_*$ and

$$h(u_*)^2 = (e^T G u_*)^2 = \frac{g_*}{\|Ae\|^2} (e^T G e) = g_* \|Ae\|^2.$$

Hence

$$\begin{aligned}
L(u_*) &= \tilde{c}g(u_*) - \tilde{\eta}h(u_*) - \mathbb{E}_t[\phi_t(g(u_*))] \\
&= \tilde{c}g_* - \tilde{\eta}g_*\|Ae\|^2 - \mathbb{E}_t[\phi_t(g_*)] \\
&= (\tilde{c} - \tilde{\eta}\|Ae\|^2)g_* - \mathbb{E}_t[\phi_t(g_*)] \\
&= \Delta g_* - \mathbb{E}_t[\phi_t(g_*)] \\
&= \Psi(g_*).
\end{aligned}$$

The only other cases include $h_* = u_* + v$ for $v \in \ker(A)$ since these are precisely the equality cases of the generalized Cauchy-Schwarz inequality. Note that for such h_* ,

$$g(h_*) = (h_*)^T G h_* = (u_* + v)^T G (u_* + v) = g(u_*) + 2v^T G u_* + v^T G v = g_*$$

and $h(u_* + v) = e^T G (u_* + v) = h(u_*)$. These cases are also global minimizers, which gives us the total set of globally optimal solutions:

$$\Theta_* := \left\{ \pm \sqrt{\frac{\sigma^2 + \|Ae\|^2}{\|Ae\|^2}} e \right\} + \ker(A).$$

Finally, we consider the Wasserstein distance bound. Note that for any $u \neq 0$, we have that

$$\begin{aligned}
W_2^2(\mathcal{N}(0, ee^T), \mathcal{N}(0, uu^T)) &= \text{tr} \left(ee^T + uu^T - 2 \left((uu^T)^{1/2} ee^T (uu^T)^{1/2} \right)^{1/2} \right) \\
&= 1 + \|u\|^2 - 2 \text{tr} \left[\left(\frac{uu^T}{\|u\|} ee^T \frac{uu^T}{\|u\|} \right)^{1/2} \right] \\
&= 1 + \|u\|^2 - 2 \text{tr} \left[\left(\frac{(e^T u)^2}{\|u\|^2} uu^T \right)^{1/2} \right] \\
&= 1 + \|u\|^2 - 2 \text{tr} \left[\frac{|e^T u|}{\|u\|^2} uu^T \right] \\
&= 1 + \|u\|^2 - 2|e^T u|.
\end{aligned}$$

In our case, note that $u_* = q \pm \lambda_* e$ where $q \in \ker(A)$ and $\lambda_* = \sqrt{1 + \sigma^2/\|Ae\|^2} > 1$. Since $e \in \text{Im}(A^T)$, $e^T q = 0$. Hence $|e^T u_*| = \lambda_*$ and $\|u_*\|^2 = \|q\|^2 + \lambda_*^2$ where we used $\|e\| = 1$ in both equalities. Using the previous result and these properties of u_* , we see that for any $u_* \in \Theta_*$,

$$W_2^2(\mathcal{N}(0, ee^T), \mathcal{N}(0, u_* u_*^T)) = 1 + \|q\|^2 + \lambda_*^2 - 2\lambda_* = \|q\|^2 + (\lambda_* - 1)^2.$$

The minimum norm element of Θ_* is precisely given by either $\lambda_* e$ or $-\lambda_* e$. This is because e and q are orthogonal for any $q \in \ker(A)$, so for any $u_* \in \Theta_*$, $\|u_*\|^2 = \lambda_*^2 \|e\|^2 + \|q\|^2 \geq \lambda_*^2 = \|\lambda_* e\|^2$. Taking $q = 0$ minimizes the norm of $u_* \in \Theta_*$. \square

E Phase I: Variants of Pretraining Details

In Section 3.1 and Section 5.1, we introduced four variants of diffusion model pretraining methods. Here, we provide the training details for each of these variants.

E.1 Standard Diffusion

Standard Diffusion aims to learn the distribution of $y^{(i)} = \mathcal{A}(x^{(i)})$ directly. To do this, we train the diffusion model on the corrupted dataset $\{y^{(i)}\}_{i=1}^N$. The training objective is given by:

$$\mathcal{L}_{\text{SD}} = \mathbb{E}_{t,y,\varepsilon} \left[\lambda(t) \|f_\phi(y + \sigma_t \varepsilon, t) - y\|_2^2 \right], \quad (7)$$

where $\lambda(t)$ is a time-dependent weighting function and σ_t is sampled from a predefined noise schedule.

The detailed training procedure is summarized in Algorithm 1.

Algorithm 1 Standard Diffusion Training

```

1: procedure STANDARD-DIFFUSION( $\{y^{(i)}\}_{i=1}^N, \sigma, p(\sigma_t), K$ )
2:   for  $k = 1$  to  $K$  do
3:     Sample a batch  $y \sim \{y^{(i)}\}_{i=1}^N$ 
4:     Sample noise level  $\sigma_t \sim p(\sigma_t)$ 
5:     Sample noise  $\varepsilon \sim \mathcal{N}(0, I_d)$ 
6:     Construct noisy input:  $y_t = y + \sigma_t \cdot \varepsilon$ 
7:     Update parameters  $\phi$  via gradient descent on  $\mathcal{L}_{\text{SD}}$  (Eq. 7)
8:   end for
9:   return Trained diffusion model  $f_\phi$ 
10: end procedure

```

E.2 Ambient Tweedie Diffusion

Ambient Tweedie Diffusion aims to learn the distribution of $\mathcal{A}(x^{(i)})$ from noisy observations $y^{(i)} = \mathcal{A}(x^{(i)}) + \sigma \cdot \varepsilon$, where σ is a known constant noise level. The goal of this pretraining objective is to mitigate the impact of additive noise during training. Similar denoising strategies have been employed in [6] and [11].

Notably, the Tweedie adjustment is compatible with more advanced diffusion training techniques, such as those presented in Appendix E.3 and Appendix E.4, which are specifically designed for random inpainting and Fourier-space inpainting tasks, respectively.

The training loss used for Ambient Tweedie Diffusion is defined as:

$$\mathcal{L}_{\text{AT}} = \mathbb{E}_{t,y,\varepsilon} \left[\left\| \frac{\sigma_t^2 - \sigma^2}{\sigma_t^2} f(y_t, t) + \frac{\sigma^2}{\sigma_t^2} y_t - y \right\|_2^2 \right], \quad (8)$$

where σ_t is sampled from the diffusion noise schedule and clipped to be no smaller than σ .

This approach introduces differences in both the training and inference procedures. Full details are provided in Algorithm 2 and Algorithm 3.

Algorithm 2 Ambient Tweedie Diffusion Training

```
1: procedure AMBIENT-TWEEDIE-TRAINING( $\{y^{(i)}\}_{i=1}^N, \sigma, p(\sigma_t), K$ )
2:   for  $k = 1$  to  $K$  do
3:     Sample batch  $y \sim \{y^{(i)}\}_{i=1}^N, \sigma_t \sim p(\sigma_t), \varepsilon \sim \mathcal{N}(0, I_d)$ 
4:      $\sigma_t \leftarrow \max\{\sigma, \sigma_t\}$  ▷ Clip noise level
5:      $y_t \leftarrow y + \sqrt{\sigma_t^2 - \sigma^2} \cdot \varepsilon$ 
6:     Update  $f_\phi$  via gradient descent on  $\mathcal{L}_{AT}$  in Eq. 8
7:   end for
8:   return Trained diffusion model  $f_\phi$ 
9: end procedure
```

Algorithm 3 Ambient Tweedie Diffusion Sampling

```
1: procedure AMBIENT-TWEEDIE-SAMPLING( $f_\phi, \sigma, \{\sigma_t\}_{t=0}^T$ )
2:   Sample  $x_T \sim \mathcal{N}(0, \sigma_T^2 I_d)$ 
3:   for  $t = T, T-1, \dots, 1$  do
4:      $\hat{x}_0 \leftarrow f_\phi(x_t, t)$ 
5:     if Truncation is applied and  $\sigma_{t-1} < \sigma$  then
6:       return  $\hat{x}_0$ 
7:     end if
8:      $x_{t-1} \leftarrow x_t - \frac{\sigma_t - \sigma_{t-1}}{\sigma_t}(x_t - \hat{x}_0)$ 
9:   end for
10: end procedure
```

E.3 Ambient Diffusion Training for Random Inpainting Task

Daras et al. [8] introduced a diffusion training objective specifically designed for the random inpainting task. The goal is to learn the underlying clean data distribution p_X from partial observations of the form $y^{(i)} = Mx^{(i)}$, where M is a binary inpainting mask applied to the image. To introduce further stochasticity, a secondary corruption mask \tilde{M} is applied during training.

The training loss for random inpainting is given by:

$$\mathcal{L}_{RI} = \mathbb{E}_{t,y,\varepsilon} \left[\left\| M f_\phi(\tilde{M}, \tilde{M}y_t, t) - y \right\|_2^2 \right], \quad (9)$$

where $y_t = y + \sigma_t \varepsilon$, and f_ϕ is conditioned on both the corrupted observation and the masking pattern.

The full training procedure is outlined in Algorithm 4.

Algorithm 4 Ambient Diffusion Training for Random Inpainting

```
1: procedure AMBIENT-INPAINTING-TRAINING( $\{y^{(i)}\}_{i=1}^N, M, p(\sigma_t), K$ )
2:   for  $k = 1$  to  $K$  do
3:     Sample batch  $y \sim \{y^{(i)}\}_{i=1}^N$ 
4:     Sample noise level  $\sigma_t \sim p(\sigma_t)$ 
5:     Sample noise  $\varepsilon \sim \mathcal{N}(0, I_d)$ 
6:     Sample a further corruption mask  $\tilde{M}$  conditioned on  $M$ 
7:     Compute  $y_t \leftarrow y + \sigma_t \cdot \varepsilon$ 
8:     Update  $f_\phi$  using gradient descent on  $\mathcal{L}_{RI}$  in Eq. 9
9:   end for
10:  return Trained diffusion model  $f_\phi$ 
11: end procedure
```

E.4 Ambient Diffusion Training for Fourier Space Inpainting

[2] introduced a diffusion training objective specifically designed for the multi-coil MRI on Fourier Space. The goal is to learn the underlying clean data distribution p_X from

$$y = \underbrace{\left(\sum_{i=1}^{N_c} S_i^H \mathcal{F}^{-1} M \mathcal{F} S_i \right)}_{\mathcal{A}} x,$$

where S_i denotes the coil sensitivity profile of the i -th coil, \mathcal{F} is the Fourier transform, and M is the masking operator in Fourier space. The further corrupted observation would be

$$\tilde{y} = \underbrace{\left(\sum_{i=1}^{N_c} S_i^H \mathcal{F}^{-1} \tilde{M} \mathcal{F} S_i \right)}_{\tilde{\mathcal{A}}} x.$$

The training loss for multi-coil MRI is given by:

$$\mathcal{L}_{\text{FS}} = \mathbb{E}_{t,y,\varepsilon} \left[\left\| \mathcal{A}(f_\phi(\tilde{y}_t, \tilde{M}, t) - y) \right\|_2^2 \right], \quad (10)$$

where $y_t = y + \sigma_t \varepsilon$, and f_ϕ is conditioned on both the corrupted observation and the masking pattern.

The full training procedure is outlined in Algorithm 5.

Algorithm 5 Ambient Diffusion Training for Fourier Space Inpainting

- 1: **procedure** AMBIENT-INPAINTING-TRAINING($\{y^{(i)}\}_{i=1}^N, M, p(\sigma_t), K, S$)
 - 2: **for** $k = 1$ to K **do**
 - 3: Sample batch $y \sim \{y^{(i)}\}_{i=1}^N$
 - 4: Sample noise level $\sigma_t \sim p(\sigma_t)$
 - 5: Sample noise $\varepsilon \sim \mathcal{N}(0, I_d)$
 - 6: Sample a further corruption mask \tilde{M} conditioned on M
 - 7: Compute $y_t \leftarrow y + \sigma_t \cdot \varepsilon$
 - 8: Update f_ϕ using gradient descent on \mathcal{L}_{RI} in Eq. 10
 - 9: **end for**
 - 10: **return** Trained diffusion model f_ϕ
 - 11: **end procedure**
-

F Phase II: Distillation phase for RSD

F.1 Distillation loss

In Section 2.3, we introduced the generator loss formulation given by Eq. 5. However, since Eq. 5 cannot be directly used for training the generator, it must be instantiated.

As discussed in Section 5, we adopt the SiD [52] distillation method, which employs Fisher divergence as the metric for distribution alignment. This choice is motivated by SiD’s superior performance compared to other distillation methods such as SDS [28] and DMD [42, 46].

For completeness, we present the corresponding generator loss formulations below. We defer implementation details—such as time-step scheduling and hyperparameter selection—to the original works.

The generator loss in the SiD framework is defined as:

$$\begin{aligned} \mathcal{L}_{\text{SiD}}(w_g) = \mathbb{E}_{z,t,w_t,\varepsilon} & \left[(1 - \alpha) \lambda(t) \|f_\psi(w_t, t) - f_\phi(w_t, t)\|_2^2 \right. \\ & \left. + \lambda(t) (f_\phi(w_t, t) - f_\psi(w_t, t))^T (f_\psi(x_t, t) - w_g) \right], \end{aligned} \quad (11)$$

where $w_t = w_g + \sigma_t \varepsilon$, with $\varepsilon \sim \mathcal{N}(0, I_d)$. Here, f_ϕ denotes the teacher (pretrained diffusion model), and f_ψ denotes the student or distilled model. The function $\lambda(t)$ is a time-dependent weighting schedule, and α is a tunable balancing parameter. In all of our experiments, we set $\alpha = 1.2$, as the SiD framework demonstrates that this value yields the best performance across a range of tasks and α settings.

F.2 Distillation Algorithm

In this section, we describe how to perform distillation after obtaining a pretrained diffusion model using various corruption-aware training losses, as introduced in Appendix E, Section 3.1, and Section 5.1. Our goal is to show how Restoration Score Distillation (RSD) accommodates different variants of pretraining and enhances the ability to generate high-quality clean images. The Algorithm details are shown in Algorithm 6.

Algorithm 6 Restoration Score Distillation (RSD)

```
1: procedure RESTORATION-SCORE-DISTILLATION( $\{y^{(i)}\}_{i=1}^N, \mathcal{A}, \sigma, K$ )
2:   # Phase I: Corruption-Aware Pretraining
3:   if  $\sigma = 0$  then
4:     Pretrain  $f_\phi(\cdot, t)$  using Algorithm 1, Algorithm 4, or Algorithm 5
5:   else
6:     Pretrain  $f_\phi(\cdot, t)$  using Algorithm 2           ▷ Denoised using Ambient Tweedie (Alg. 2)
7:   end if
8:
9:   # Phase II: One-Step Generator Distillation
10:  Initialize surrogate diffusion model  $f_\psi \leftarrow f_\phi$  and one-step generator  $G_\theta \leftarrow f_\phi$ 
11:  for  $j = 1$  to  $K$  do
12:     $x_g \leftarrow G_\theta(z), \quad z \sim \mathcal{N}(0, I_d)$ 
13:     $\tilde{y}_g \leftarrow \mathcal{A}(x_g) + \sigma \cdot \epsilon, \quad \epsilon \sim \mathcal{N}(0, I_d)$            ▷ Corrupt the same manner as dataset
14:    Gradient update on  $f_\psi(\cdot, t)$  on the same pretraining loss used for  $f_\phi$ , with input  $\tilde{y}_g$ 
15:
16:     $x_g \leftarrow G_\theta(z), \quad z \sim \mathcal{N}(0, I_d)$ 
17:     $w_g \leftarrow \mathcal{A}(x_g)$            ▷ Denoising is already handled by Ambient Tweedie (see Alg. 2)
18:    Update  $G_\theta$  via a gradient step on the generator loss in Eq. (11) using  $w_g$ 
19:  end for
20: end procedure

1: procedure RESTORATION-SCORE-DISTILLATION-GENERATION
2:   # One-Step Inference
3:    $x_g \leftarrow G_\theta(z), \quad z \sim \mathcal{N}(0, I_d)$ 
4:   return  $x_g$ 
5: end procedure
```

G Implementation Details

G.1 Training

Pretraining. We follow the EDM training setup [20] and train for 100 million image iterations during the pretraining phase. For the Gaussian deblurring and super-resolution tasks with $\sigma = 0$, we use the Standard Diffusion objective (Eq. 7). For the same tasks with $\sigma = 0.2$, we adopt the Ambient Tweedie loss (Eq. 8) for pretraining.

For the random inpainting task with $\sigma = 0$, we utilize the publicly available pretrained checkpoint from <https://github.com/giannisdaras/ambient-diffusion/tree/main>. In the case of random inpainting with $\sigma = 0.2$, we also use the Ambient Tweedie loss (Eq. 8) for training. We avoid using the dedicated inpainting loss (Eq. 9) in this noisy setting, as we found it to be unstable, consistent with observations reported in [9]. For the Fourier-space random inpainting task on MRI data, we use the pretrained checkpoint provided at <https://github.com/utcsilab/ambient-diffusion-mri.git>.

All pretrained diffusion models use the same hyperparameter settings as EDM [20].

Distillation. In the distillation phase, we train the one-step generator for 50 to 100 million image iterations. Training is terminated early if we observe that the FID curve begins to diverge. All pretrained and distilled models are trained on 8 NVIDIA A100 GPUs with 80GB memory each.

G.2 Evaluation and Inference Efficiency

We generate 50,000 images to compute the FID score. Each FID value reported in this paper is calculated using images generated with seeds ranging from 0 to 49,999.

In terms of inference efficiency, using 8 A100 GPU nodes with a batch size of 64 per GPU, our model generates 50,000 images in approximately 25 seconds. In comparison, under the same hardware

and batch size conditions, sampling with 40 steps—as used in EDM for the CelebA task—requires around 500 seconds to generate the same number of images.

Table 5: Time to generate 50k images.

Method	Wall Time(seconds)
Teacher Diffusion	500
RSD(one-step)	25

G.3 Multi-Coil MRI

We follow the same setting as [2]. When pretrained diffusion checkpoints are available, our method technically does not require any MRI data samples. However, in multi-coil MRI, sensitivity maps must be provided. We obtain these maps using the ESPiRiT calibration method [40], following standard practice in the MRI literature.

G.4 Model Selection Criterion

As discussed in Section 5.3, we employ *proximal FID* as a model selection criterion. This involves computing the FID between the set $\{\mathcal{A}(x^{(i)}) + \sigma\epsilon\}_{i=1}^{50k}$ and the corrupted dataset. In this section, we report both the best true FID achieved during the training process and the true FID of the model selected using proximal FID.

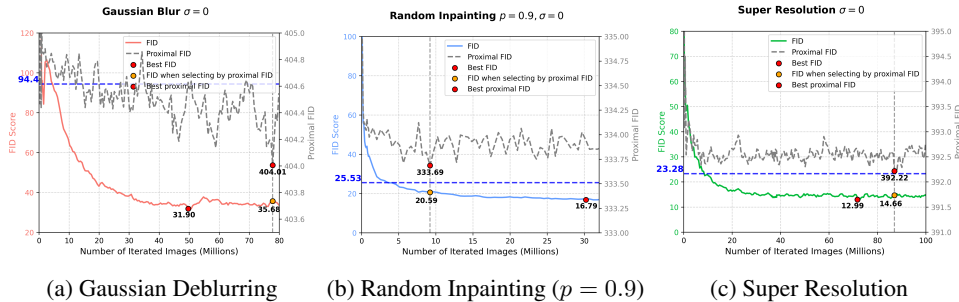


Figure 10: Comparison between true FID and proximal FID during training across different tasks.

G.5 Training Curves

In this section, we present additional training curves illustrating the performance of our method during the distillation phase. Each plot shows the FID score as a function of the number of iterated images. The horizontal line represents the performance of the corresponding teacher diffusion model, serving as a baseline reference.

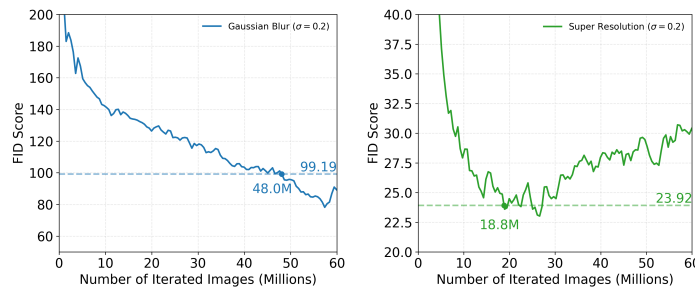


Figure 11: FID curves during distillation for (left) Gaussian Deblurring with $\sigma = 0.2$ and (right) Super Resolution with $\sigma = 0.2$. The horizontal line indicates the best FID achieved by the teacher diffusion model.

Table 6: Comparison between the best true FID and the FID of the model selected by proximal FID.

Noise (σ)	Task	Best FID	FID Selected by Proximal FID
$\sigma = 0.0$	Gaussian Deblurring	31.90	35.68
	Random Inpainting ($p = 0.9$)	16.79	20.59
	Super Resolution ($\times 2$)	12.99	14.66
$\sigma = 0.2$	Gaussian Deblurring	76.98	88.29
	Random Inpainting ($p = 0.9$)	79.48	83.98
	Super Resolution ($\times 2$)	22.00	27.42

H Additional Qualitative Examples



Figure 12: Examples from the training dataset used for the Gaussian blur task with $\sigma = 0$.

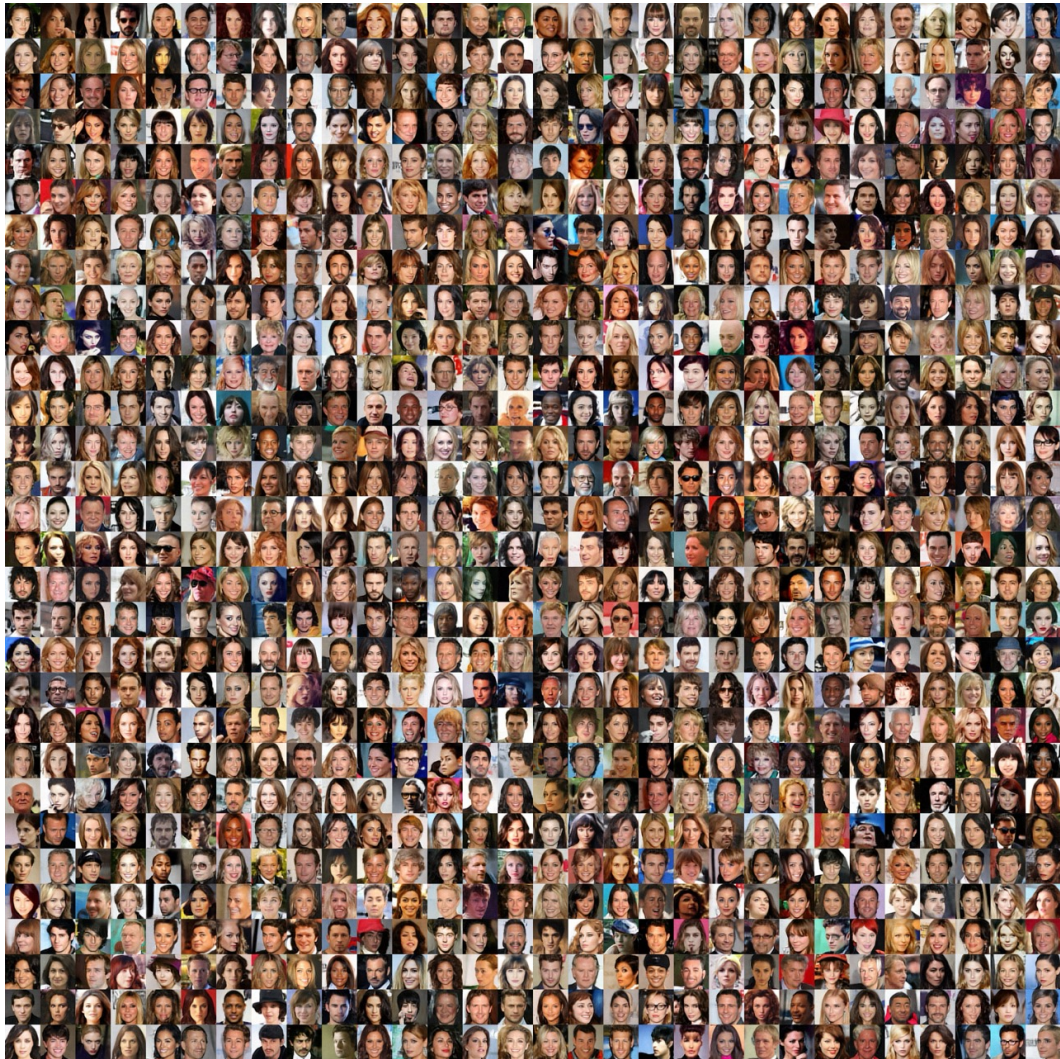


Figure 13: Qualitative results of SiD generation for the Gaussian blur task with $\sigma = 0$.

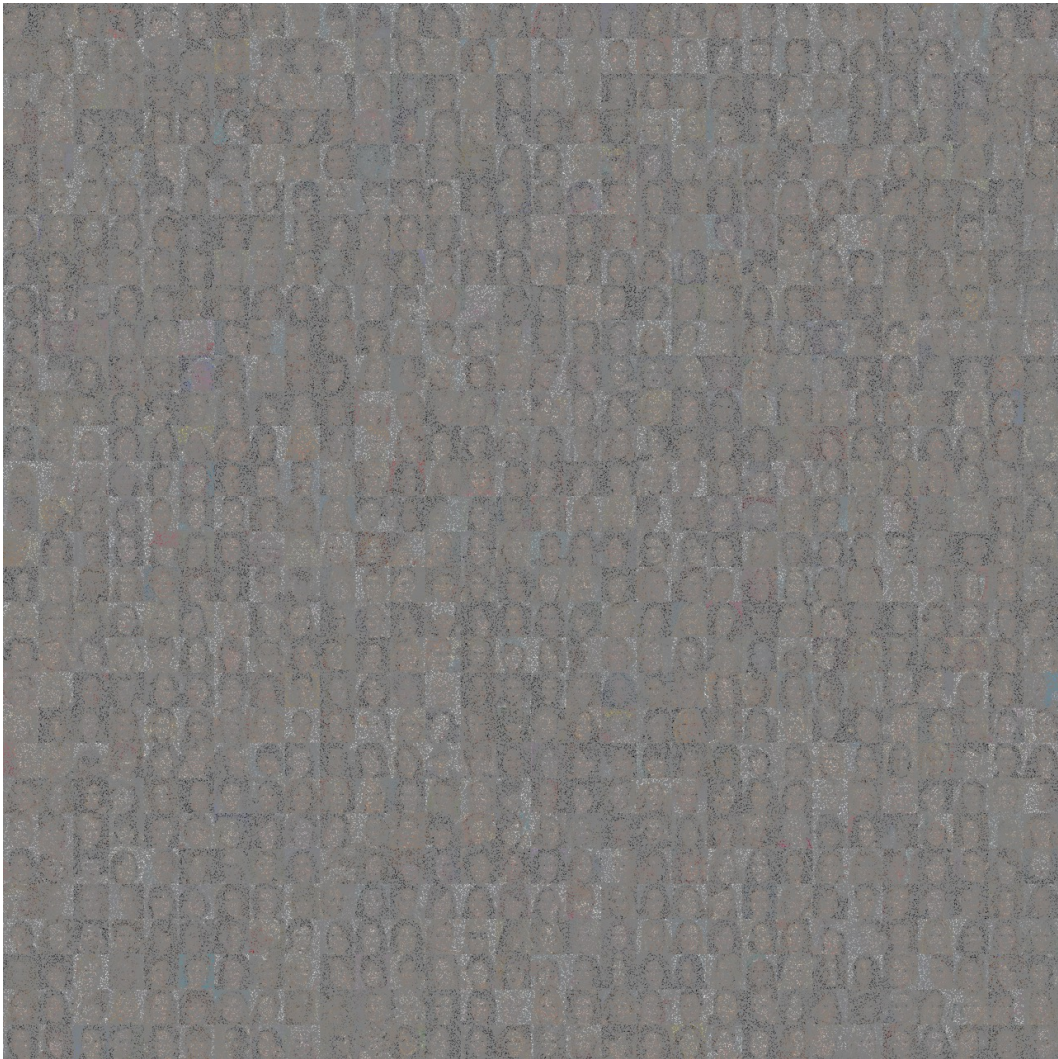


Figure 14: Dataset samples for the random inpainting task with $p = 0.9$ and $\sigma = 0$.

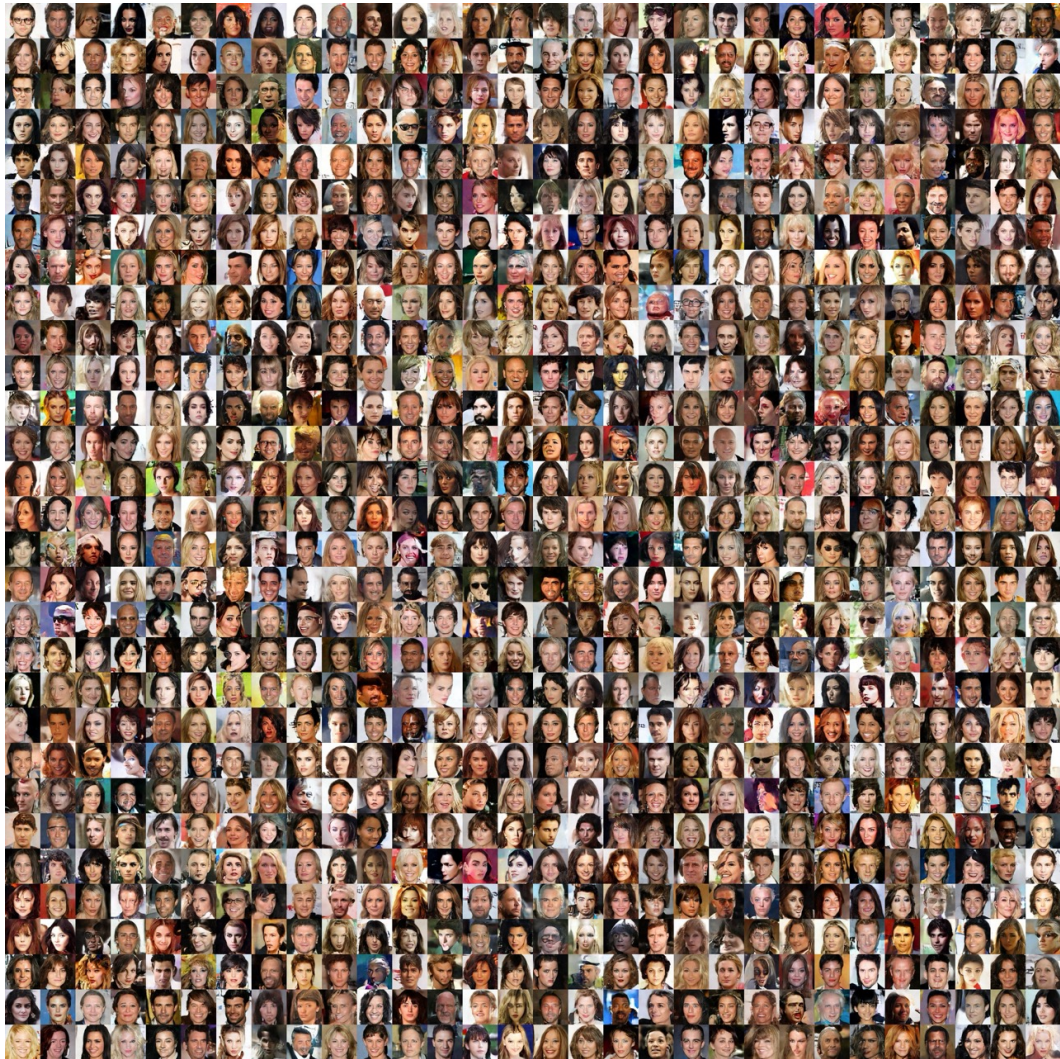


Figure 15: SiD generation results for the random inpainting task with $p = 0.9$ and $\sigma = 0$.

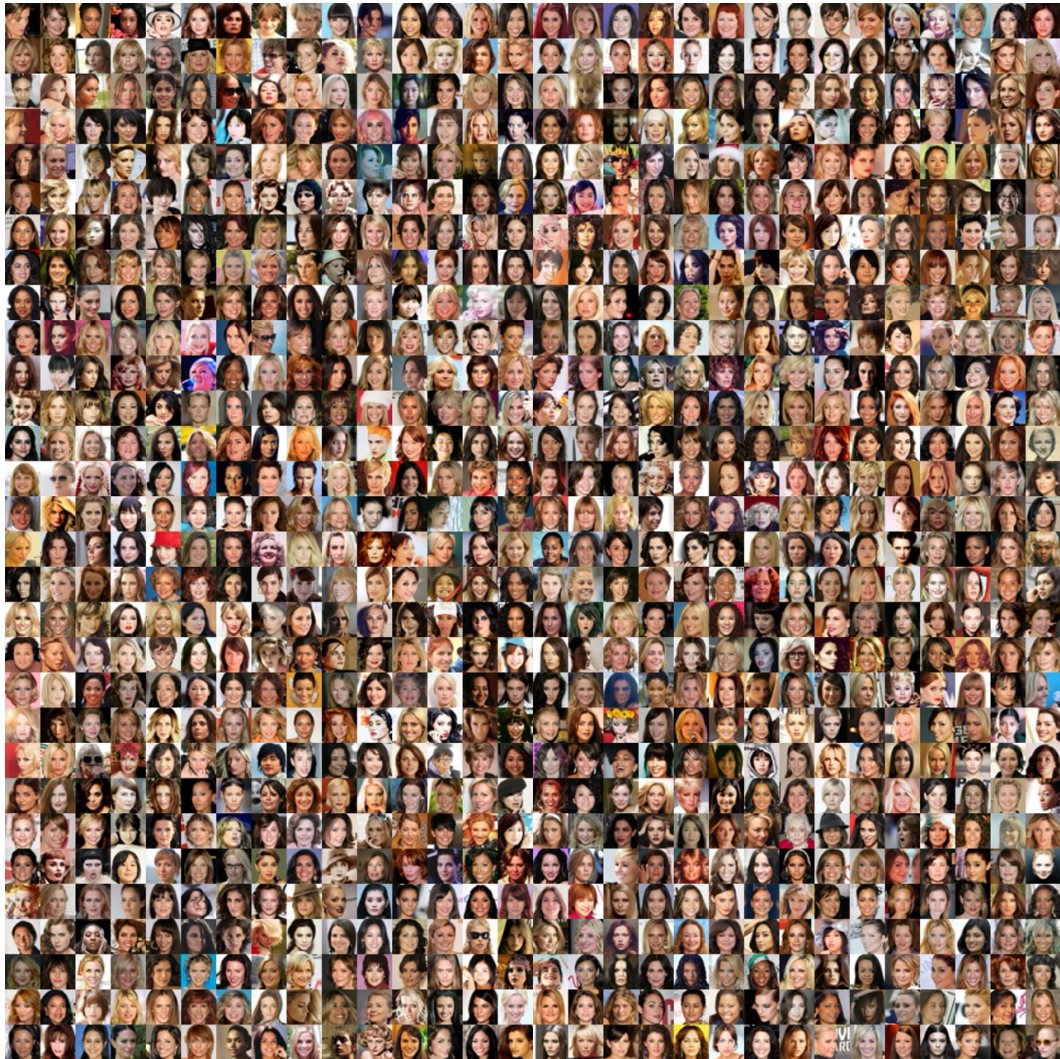


Figure 16: Dataset samples for Super Resolution $\times 2$ Task with $\sigma = 0$

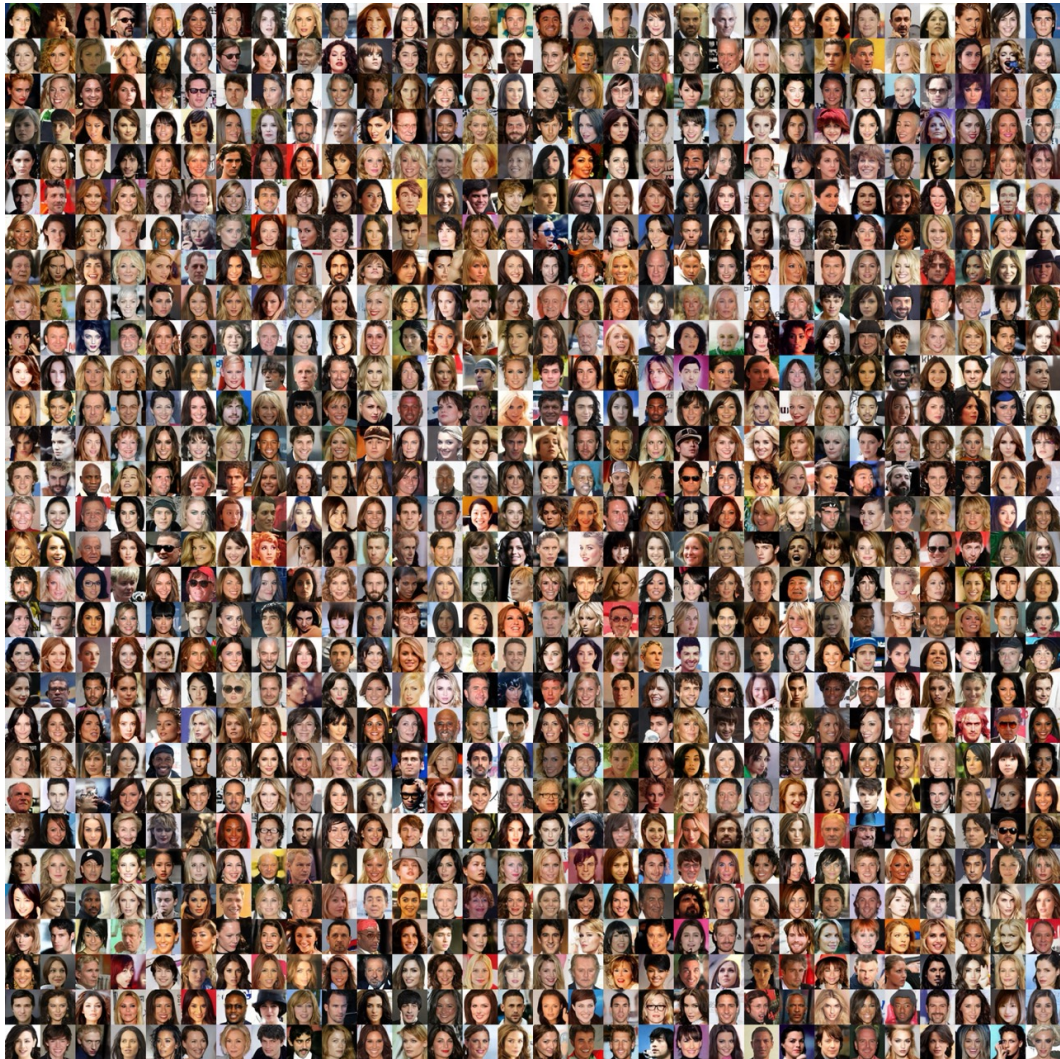


Figure 17: SiD generation results for Super Resolution $\times 2$ Task with $\sigma = 0$

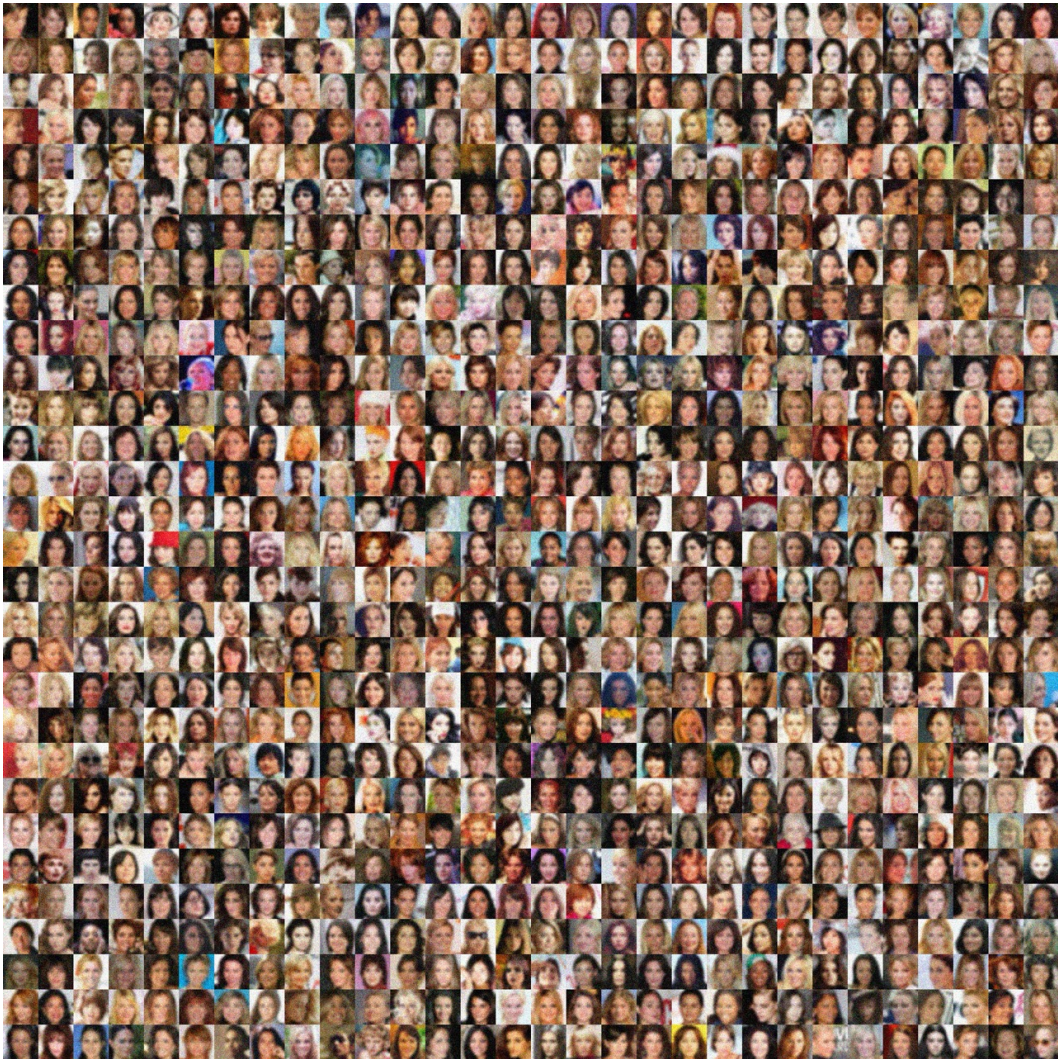


Figure 18: Dataset samples for Gaussian Blur with $\sigma = 0.2$

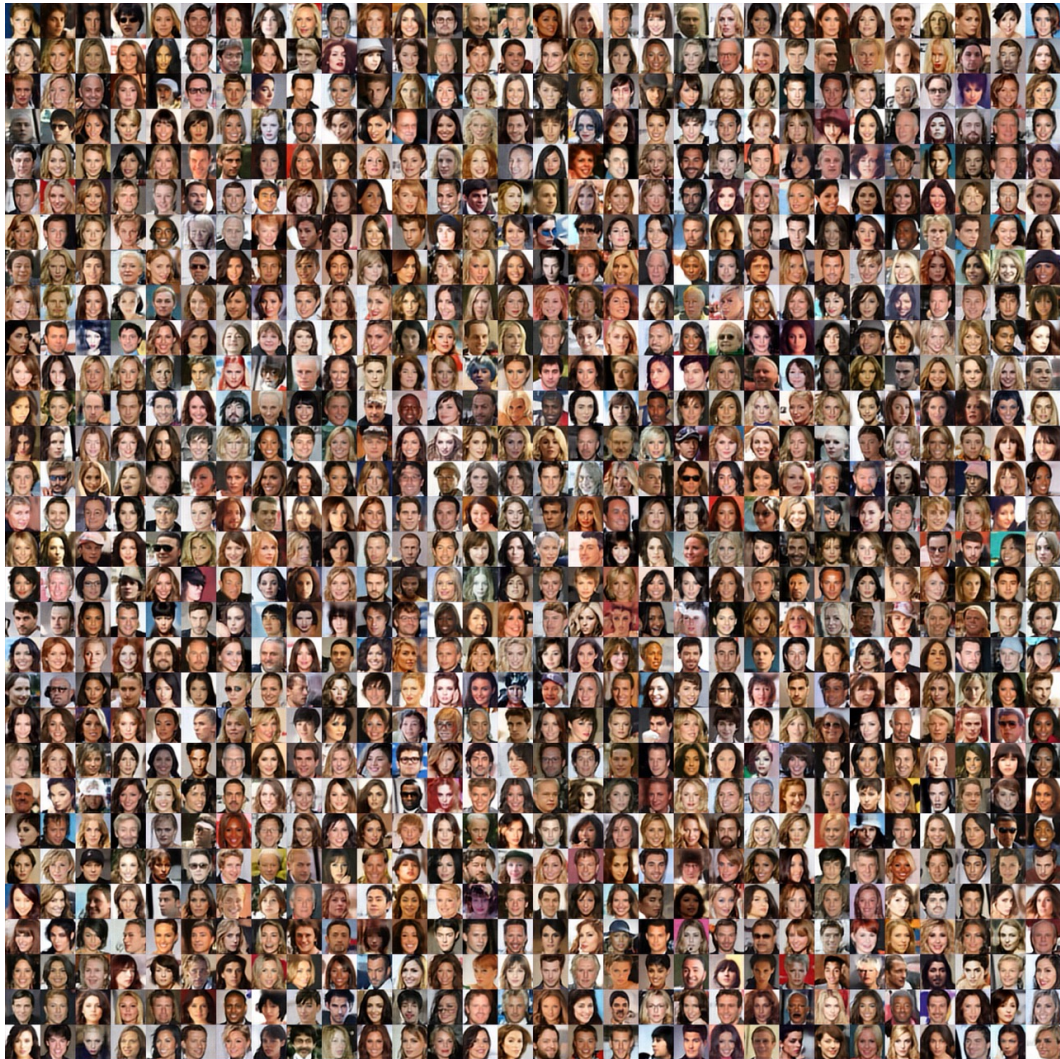


Figure 19: SiD generation results for Gaussian Blur with $\sigma = 0.2$

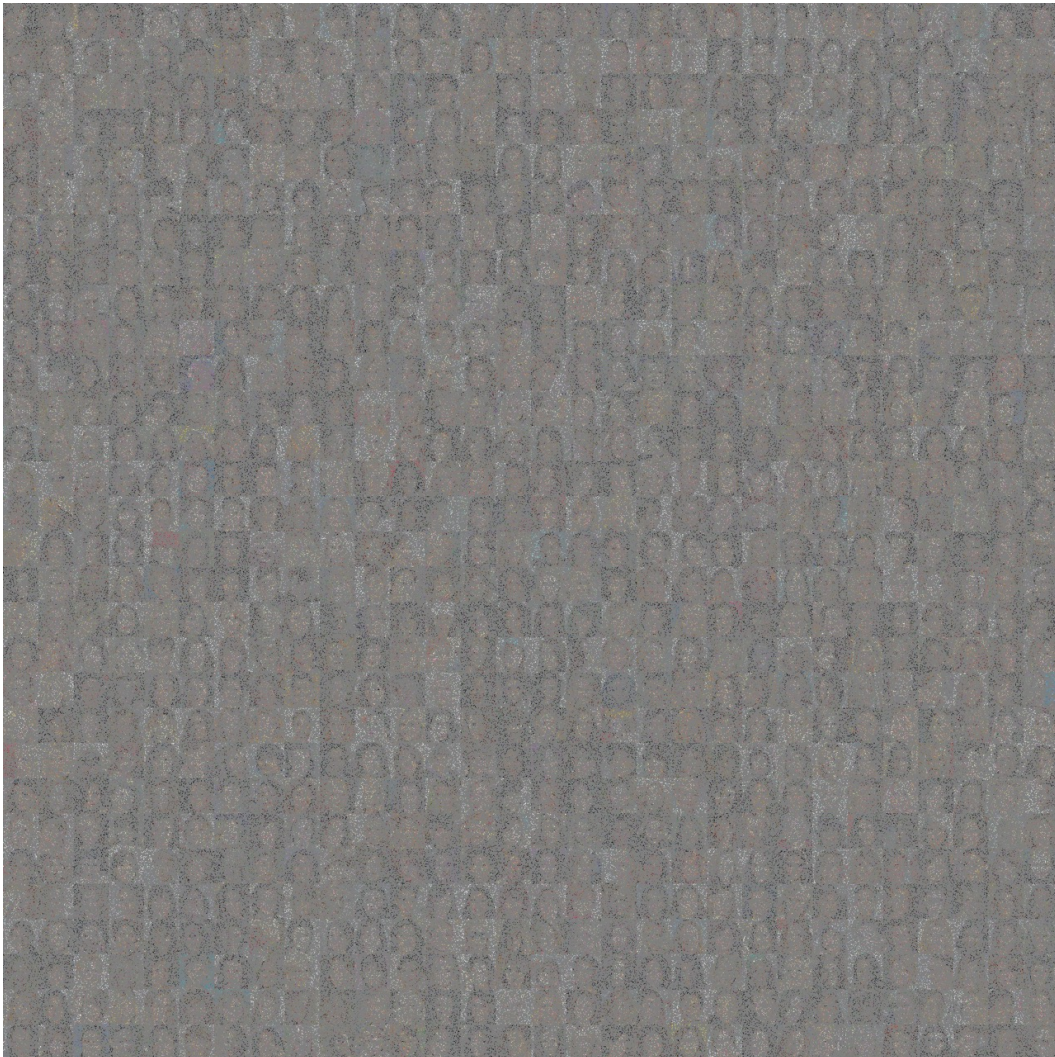


Figure 20: Dataset samples for Random Inpainting with $p = 0.9$ and $\sigma = 0.2$

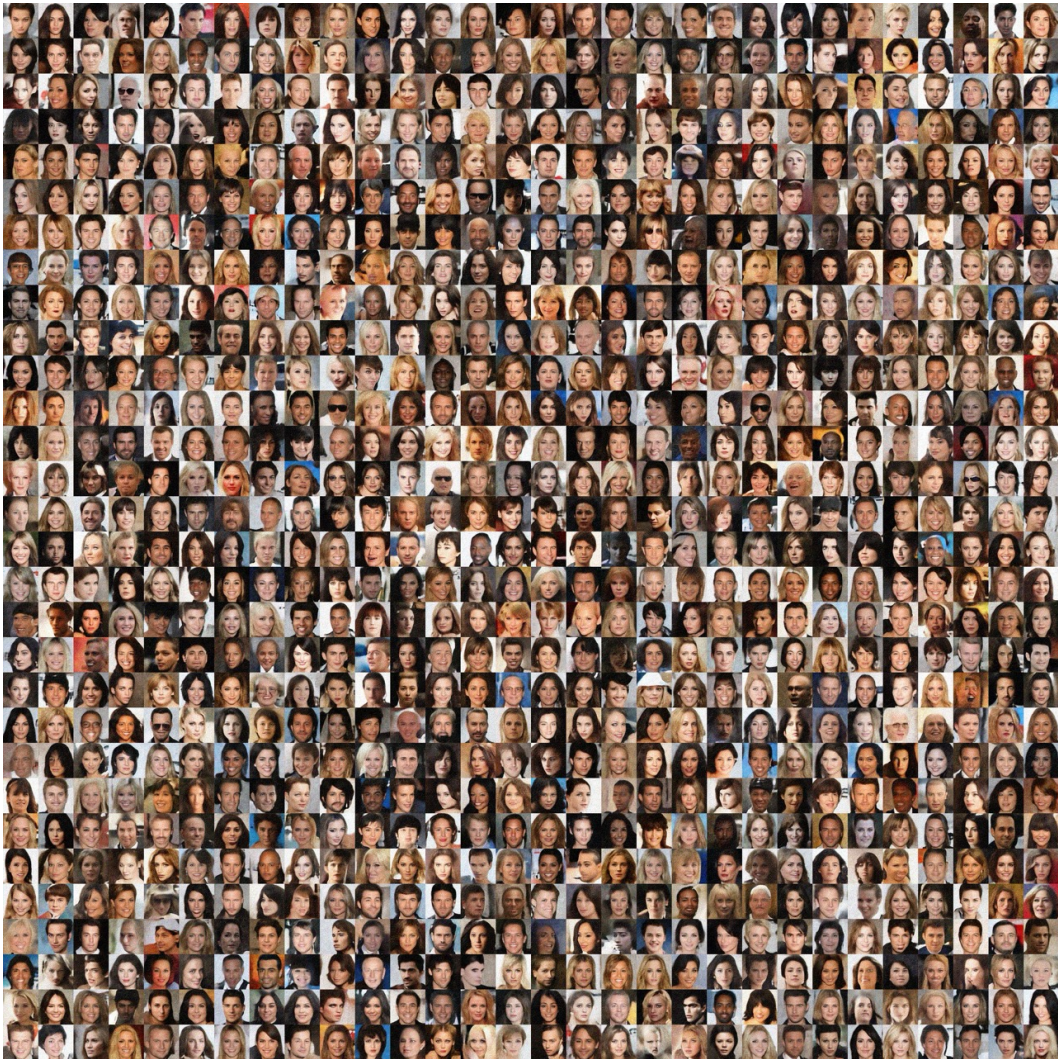


Figure 21: SiD generation results for Random Inpainting with $p = 0.9$ and $\sigma = 0.2$

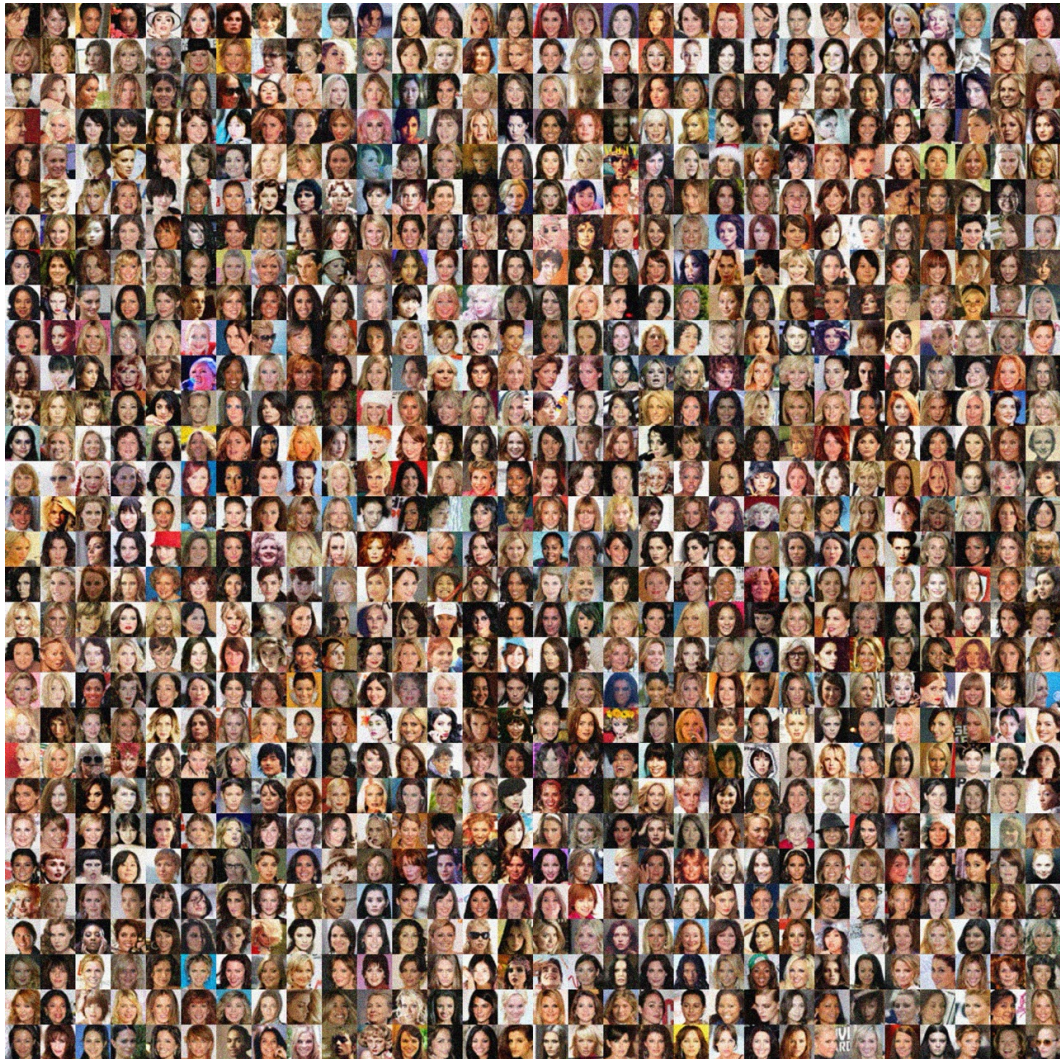


Figure 22: Dataset samples for Super Resolution $\times 2$ Task with $\sigma = 0.2$

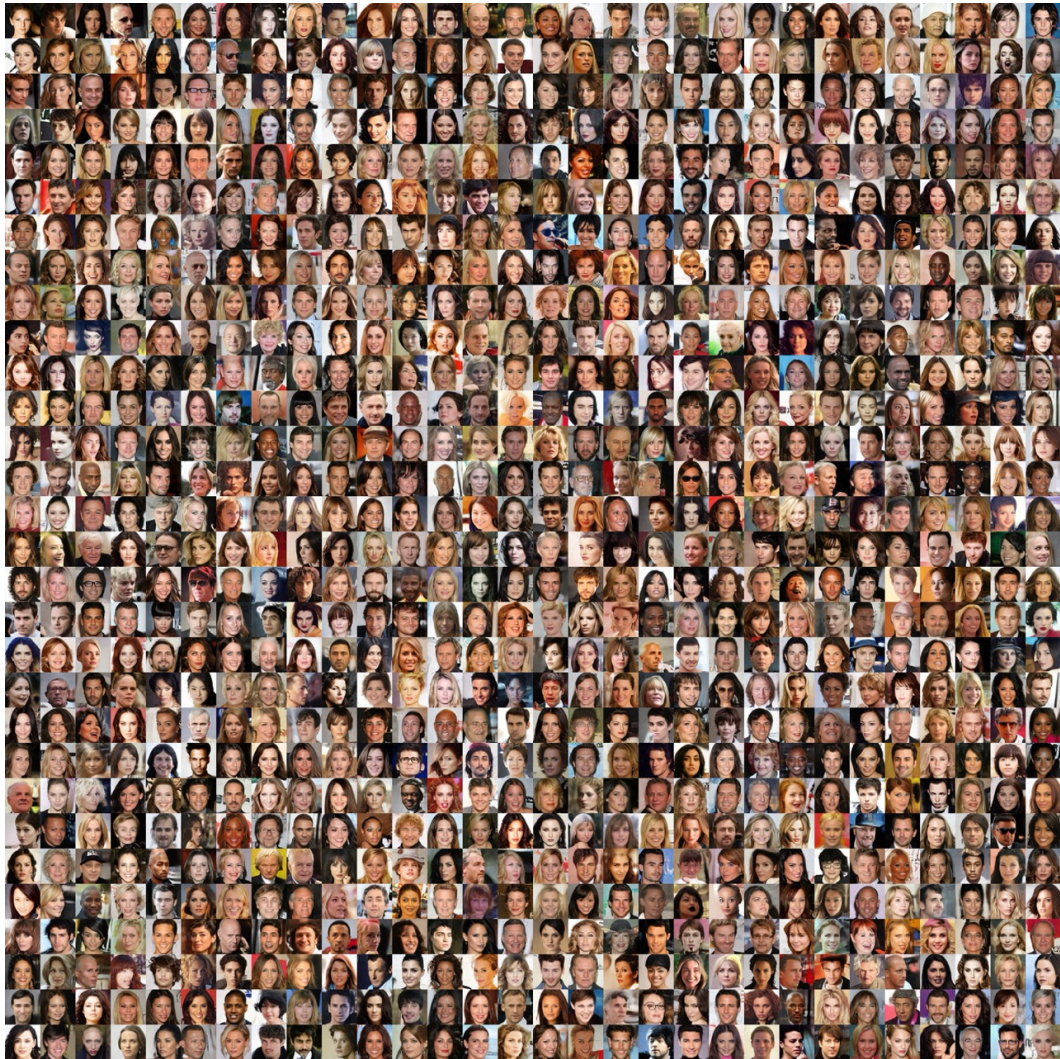


Figure 23: SiD generation results for Super Resolution $\times 2$ Task with $\sigma = 0.2$

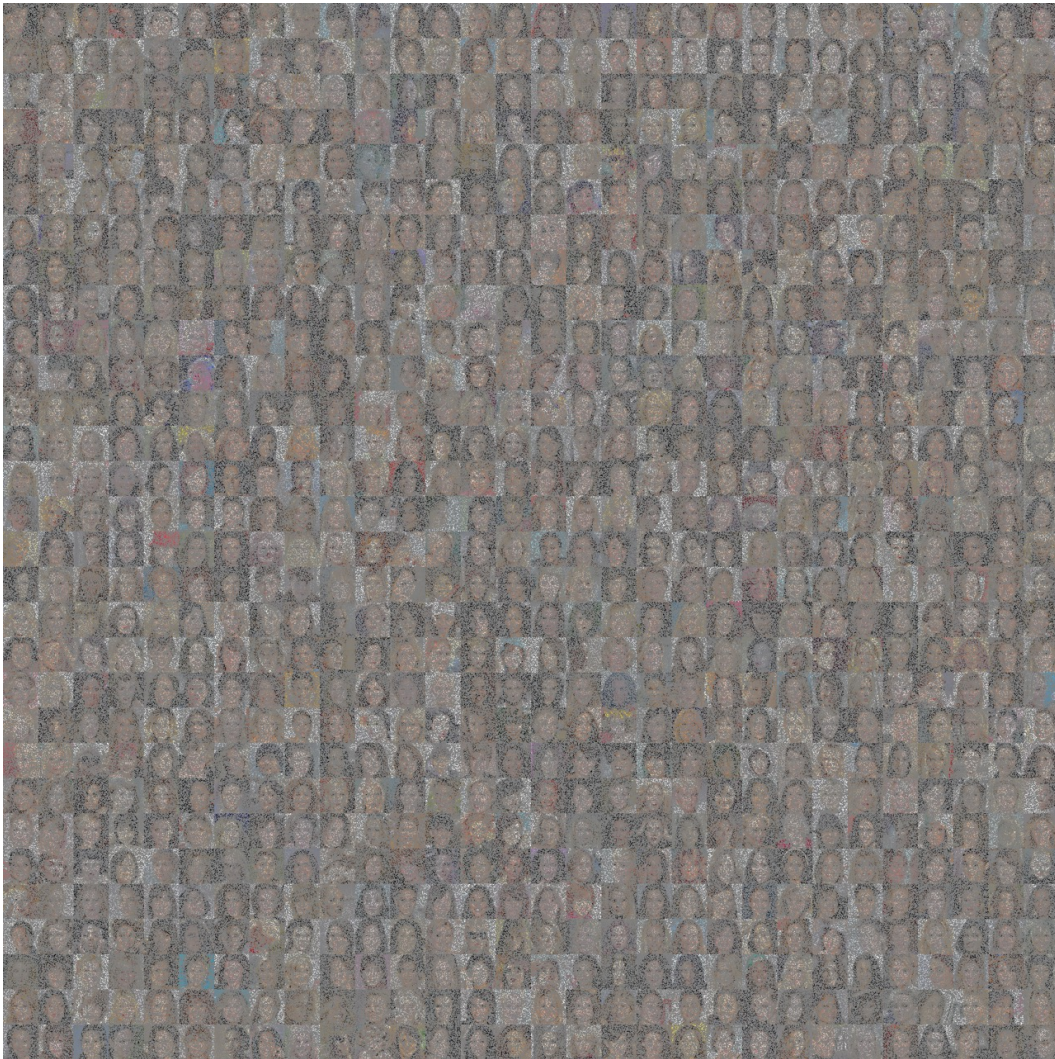


Figure 24: Dataset samples for Random Inpainting with $p = 0.8$ and $\sigma = 0$

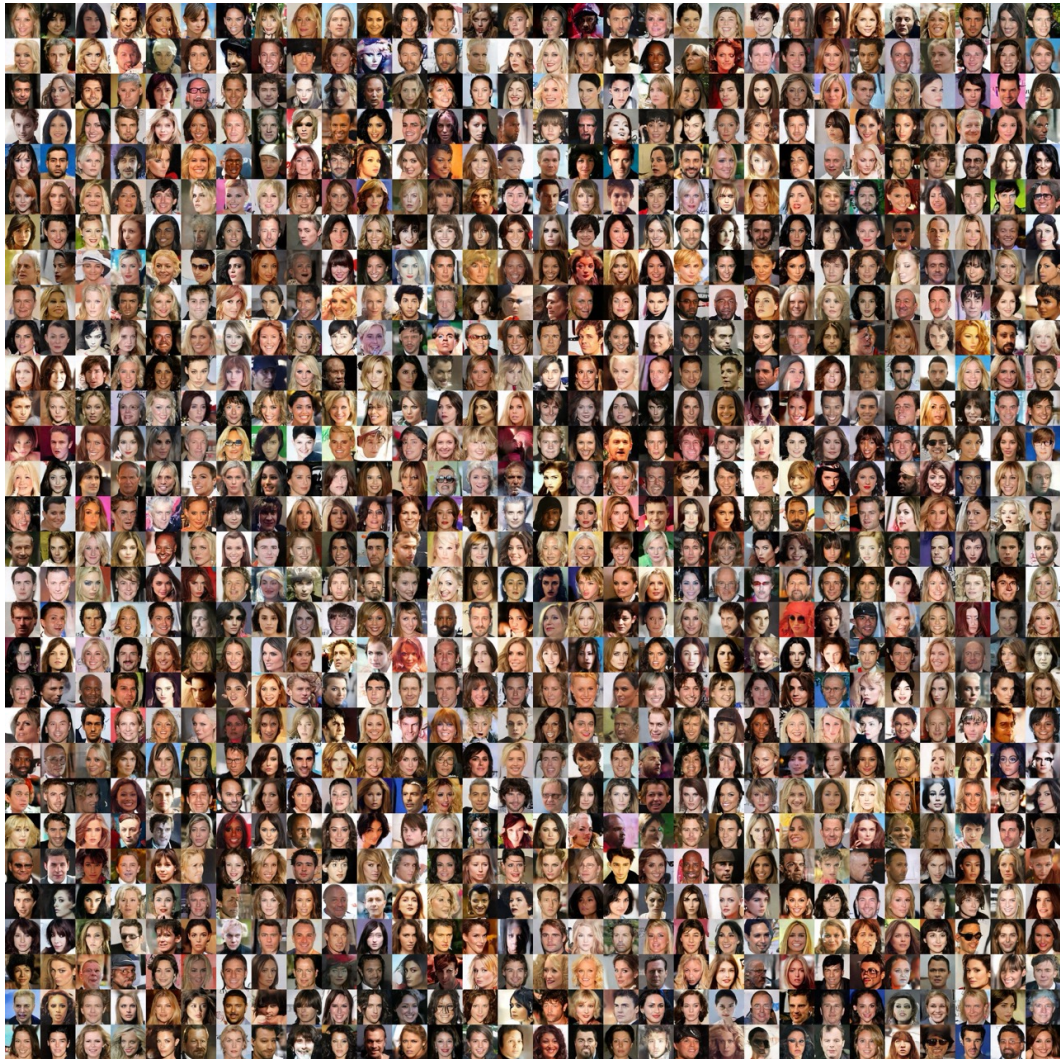


Figure 25: SiD generation results for Random Inpainting with $p = 0.8$ and $\sigma = 0$

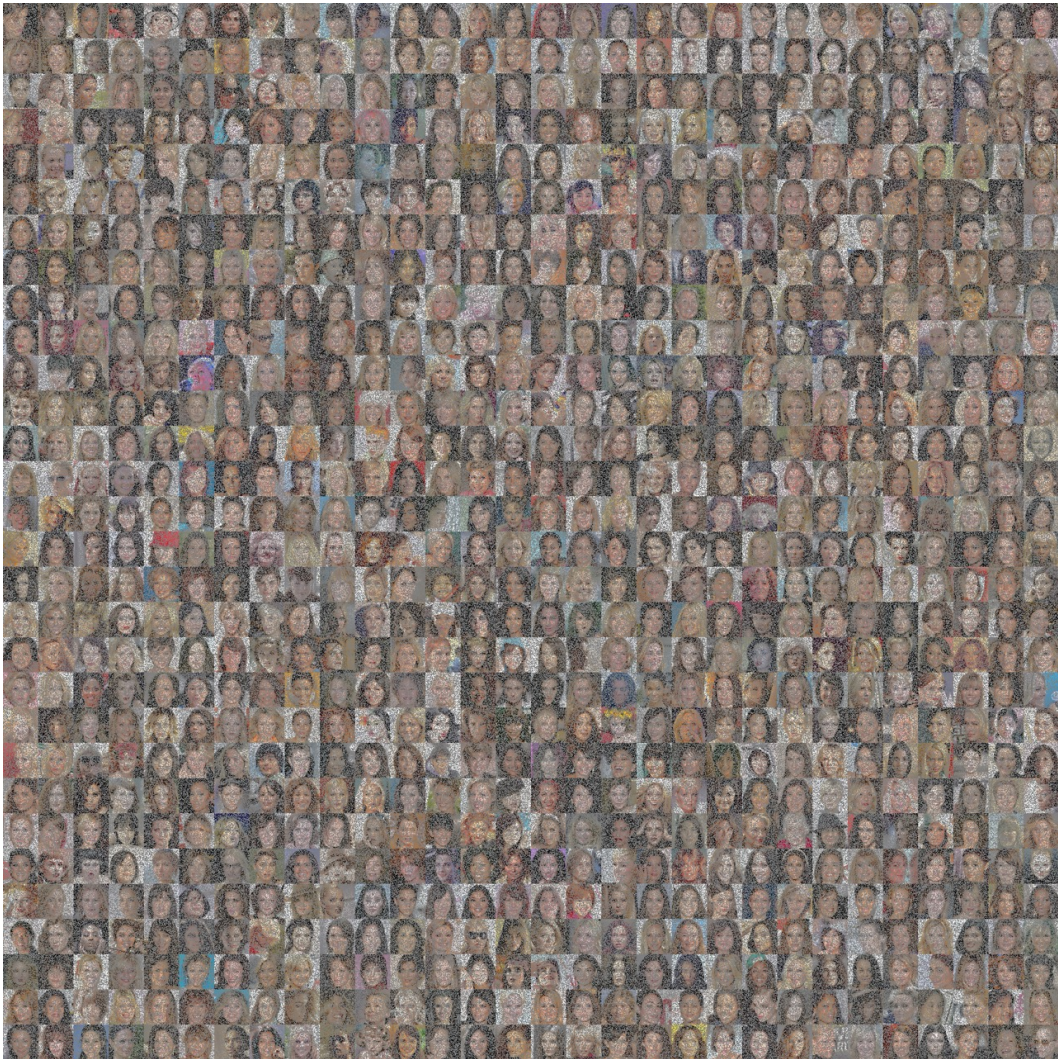


Figure 26: Dataset samples for Random Inpainting with $p = 0.6$ and $\sigma = 0$

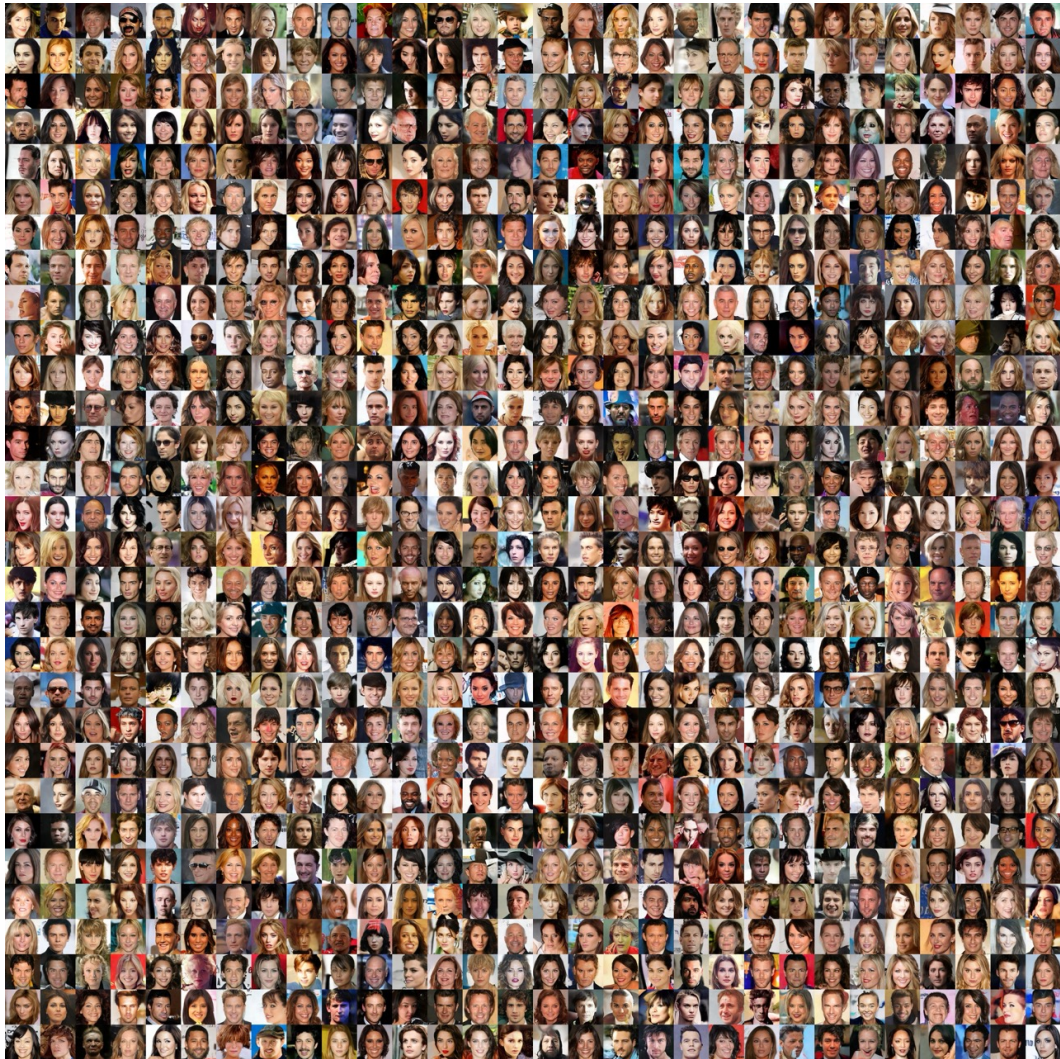


Figure 27: SiD generation results for Random Inpainting with $p = 0.6$ and $\sigma = 0$